DESIGN, ANALYSIS AND IMPLEMENTATION OF A 50 W WIRELESS CHARGER OF A CHARGING VEST BATTERY

A THESIS SUBMITTED TO
THE GRADUATE SCHOOL OF NATURAL AND APPLIED SCIENCES
OF
MIDDLE EAST TECHNICAL UNIVERSITY

BY

MERİH EREN

IN PARTIAL FULFILLMENT OF THE REQUIREMENTS
FOR
THE DEGREE OF MASTER OF SCIENCE
IN
ELECTRICAL AND ELECTRONICS ENGINEERING

DECEMBER 2019

Approval of the thesis:

DESIGN, ANALYSIS AND IMPLEMENTATION OF A 50 W WIRELESS CHARGER OF A CHARGING VEST BATTERY

submitted by **MERİH EREN** in partial fulfillment of the requirements for the degree of **Master of Science in Electrical and Electronics Engineering Department, Middle East Technical University** by,

Prof. Dr. Halil Kalıpçılar
Dean, Graduate School of **Natural and Applied Sciences** ______________

Prof. Dr. İlkay Ulusoy
Head of Department, **Electrical and Electronics Engineering** ______________

Assist. Prof. Dr. Emine Bostancı
Supervisor, **Electrical and Electronics Engineering, METU** ______________

Examining Committee Members:

Prof. Dr. Işık Çadırcı
Electrical and Electronics Engineering, Hacettepe Üni. ______________

Assist. Prof. Dr. Emine Bostancı
Electrical and Electronics Engineering, METU ______________

Assoc. Prof. Dr. Murat Göl
Electrical and Electronics Engineering, METU ______________

Assist. Prof. Dr. Ozan Keysan
Electrical and Electronics Engineering, METU ______________

Assist. Prof. Dr. Taner Göktaş
Electrical and Electronics Engineering, İnönü Üni. ______________

Date: 08.12.2019

I hereby declare that all information in this document has been obtained and presented in accordance with academic rules and ethical conduct. I also declare that, as required by these rules and conduct, I have fully cited and referenced all material and results that are not original to this work.

Name, Surname: Merih Eren

Signature :

ABSTRACT

DESIGN, ANALYSIS AND IMPLEMENTATION OF A 50 W WIRELESS CHARGER OF A CHARGING VEST BATTERY

Eren, Merih
M.S., Department of Electrical and Electronics Engineering
Supervisor: Assist. Prof. Dr. Emine Bostancı

December 2019, 88 pages

Wireless power transfer (WPT) has been a very popular research topic for a variety of applications with power ratings ranging from few watts to several kilowatts. High power levels are mostly used in electric vehicle charging applications whereas lower power level applications are mostly in household appliances, wearable devices and medical implants. Topology, geometries of the transferring and receiving coils and their relative positions are fundamental parts that affect performance of WPT systems. In WPT systems, the most common problem is the degradation of the performance in case of a misalignment of the transferring and receiving coils. Moreover, shielding of the magnetic field is high of importance for on body charging systems like charging vests to meet the electromagnetic field restrictions for human tissue. In this thesis, a 50 W WPT system for battery charging in charging vests is studied in terms of topology selection and coil design. A series-series compensated type inductive power transfer topology is selected and two different coil pairs (transmitter-receiver) that correspond to different resonant frequencies are determined. These configurations are chosen by using a Pareto-front optimization approach that is applied to find out designs with a high efficiency over a wide range of frequencies and misalignments. Furthermore, performances of possible shield designs are studied by using finite element analysis for those two designs. The selected WPT systems are prototyped and tested to validate the analytical and numerical analysis results.

Keywords: Wireless Power Transfer, Inductive Power Transfer, Wireless Battery Charger, Compensation Topologies, Pareto-front, Electromagnetic Shielding

ÖZ

SARJ YELEĞİ AKÜSÜNÜN 50 W GÜCÜNDEKİ KABLOSUZ ŞARJ CİHAZININ TASARIMI, ANALİZİ VE UYGULAMASI

Eren, Merih
Yüksek Lisans, Elektrik ve Elektronik Mühendisliği Bölümü
Tez Yöneticisi: Dr. Öğr. Üyesi. Emine Bostancı

Aralık 2019 , 88 sayfa

Güç aralıkları birkaç watttan birkaç kilowatta kadar değişen kablosuz güç transferi sistemleri araştırmacılar için popüler bir araştırma konusu olmuştur. Yüksek güçlü kablosuz güç transfer sistemleri, daha çok elektrikli araç şarj sistemlerinde kullanılırken, daha düşük güçlü sistemler daha çok ev elektroniği, giyilebilir teknoloji ve medikal uygulamalarda kullanılmaktadır. Topoloji, verici ve alıcı sargıların geometrisi, ve sargıların birbirlerine göre konumları kablosuz güç transferinin performasını etkileyen en kritik noktalardır. Birçok kablosuz güç aktarma sisteminde en çok karşılaşılan problemlerden biri ise, verici ve alıcı sargılar arasındaki hiza kaymasının sistem performasında düşüşlere neden olmasıdır. Bunlara ek olarak, vücut üzerinde yapılacak sarj uygulamalarında, örnek olarak sarj yeleği gibi, insan dokusuna uygulanabilecek elektromanyetik alan sınırlarını aşmamak için kullanılacak olan elektromanyetik alan koruma kalkanı büyük önem taşımaktadır. Bu tezde kapsamında, sarj yeleği aküsünün 50 W gücündeki kablosuz şarj cihazı, topoloji seçimi ve sarımların tasarımı gibi dizayn kriterleri göz önünde bulundurularak incelenmiştir. Seri-seri kompanzasyonlu endüktif güç transferi topolojisi seçilmiş ve farklı rezonans frekanslarına sahip olan iki farklı sargı çifti (verici - alıcı) belirlenmiştir. Bu konfigurasyonlar, Pareto-front optimizasyon tekniği kullanılarak sistemin geniş frekans aralığında ve sargılar arasında mesafe değişimi durumlarında yüksek verimle çalışması amaçlanarak seçilmiştir. Oluşturulan iki farklı tasarım için, elektromanyetik alan koruma kalkanı performansları sonlu eleman yöntemi ile analiz edilmiştir. Seçilmiş olan sistemler üretilmiş ve test sonuçları analitik ve numerik analiz sonuçlarının doğrulanmasında kullanılmıştır.

Anahtar Kelimeler: Kablosuz Güç Transferi, Endüktif Güç Transferi, Kablosuz Şarj Cihazı, Kompanzasyon Topolojileri, Pareto-front, Elektromanyetik Koruma Kalkanı

To my family

ACKNOWLEDGMENTS

First, I am deeply grateful to my supervisor Assist. Prof. Dr. Emine Bostancı, for her support and encouragement. Her guidance and inspirational suggestions lead me throughout this thesis.

Besides, I would like to thank to the members of examining committee: Prof. Dr. Işık Çadırcı, Assoc. Prof. Murat Göl, Assist. Prof. Dr. Ozan Keysan and Assist. Prof. Dr. Taner Göktaş for their insightful comments and suggestions. Also, I would like to thank to Prof. Dr. Ahmet M. Hava for his precious contributions for my thesis study and especially for my engineering career.

I would like to express my gratitude to ELSİS A.Ş. for their support throughout my thesis study. Particularly, the company shareholders Behçet Tonak and Pekin Tonak's supports were priceless.

I would like to thank to Alican Madan, Oğuzhan Öztoprak and Arın Cengiz. Discussion with them have been illuminating.

I owe a very important debt to my mother Raziye Eren, my father Mehmet Eren and my sister Merve Uzun for their never-ending belief in me. I am really appreciative for their love.

Finally, I am grateful for love of my life, Filiz Biçer, for her never-ending support in every part of my life. Without her love and support, this study would not have been possible.

TABLE OF CONTENTS

LIST OF TABLES

TABLES

LIST OF FIGURES

FIGURES

LIST OF ABBREVIATIONS

ABBREVIATIONS

CPT	Capacitive Power Transfer
EM	Electromagnetic
FEA	Finite Element Analysis
HB	Half Bridge
ICNIRP	International Commission on Non-Ionizing Radiation Protection
IPT	Inductive Power Transfer
MOSFET	Metal Oxide Semiconductor Field Effect Transistor
MRPT	Magnetic Resonance Power Transfer
PP	Parallel-Parallel
PS	Parallel-Series
RF	Radio Frequency
SS	Series-Series
SP	Series-Parallel
WPT	Wireless Power Transfer
ZPA	Zero Phase Angle

CHAPTER 1

INTRODUCTION

Wireless power transfer (WPT) that has started with the efforts of Nikola Tesla have been gaining popularity in recent times [14]. Especially, with the growth in the electrical vehicle technology, wireless power transfer became a necessary technology to reduce the size of the battery and charging times. Moreover, lowering battery requirement, increasing power transfer distance, making devices more compact for other applications like medical applications and portable consumer devices are other reasons behind the developments in wireless power transfer technology.

Wireless power transfer range varies between a few centimeters to a few meters. In this range of power transfer, inductive coupling or capacitive coupling between transmitter and receiver is used. Among these couplings, inductive coupling is the mostly preferred method because of its high power transfer capability and relatively low operating frequency. On the contrary, capacitive coupling requires much higher operating frequency than inductive coupling and its power transfer distance is much lower [15]. Besides, for longer power transfer distances in kilometers range, radio frequency (RF) wireless power transfer can be applied. Its operation is different than inductive coupling such that power is transferred omnidirectional in RF based wireless power transfer systems. Therefore, transferred power efficiency of RF systems is quite low with respect to inductive power transfer [4].

Improvements in WPT have provided many eases to human life. Eliminating cables, reducing dependency to heavy and bulky batteries and providing a safer usage with its galvanic isolation can be counted as some of its advantages. In addition, one of the significant advantage is in the medical area. Suppressing battery requirement of implantable devices enables to have much compact products and it eliminates the requirement of a surgery for battery replacement.

On the contrary to the advantages of WPT, it has many challenging aspects. A foreign object such as a coin near to the magnetic fluxes may exists so the magnetic field is absorbed by the object and it may cause an excessive amount of temperature increase. Not only a metallic object, a living creature, such as a cat, may lie down between transmitter and receiver while charging batteries of a vehicle. Therefore, any foreign object must be handled by means of their effect to the WPT system and the effect of WPT system to those objects. Another important challenge is the misalignment between receiver and transmitter coils. It is not enough that receiver is close to the transmitter but its alignment with respect to transmitter is also essential. In WPT systems, receiver is usually mobile and its position with respect to transmitter varies. In order to transfer power efficiently, magnetic flux should be picked up by receiver properly and it is only possible with a proper alignment. In addition to the misalignment, shielding is another challenging point. Since WPT systems are the magnetic field source, they shouldn't interfere with any electrical device or cause harm to a living creature. Therefore, they must be compliant with safety standards and electromagnetic compatibility restrictions.

1.1 Scope of the Thesis

The aim of this study is to design and test a 50W wireless charging system for a battery in a charging vest. The challenges associated with this application are the need for a compact, effective and safe design.

Importance of the compactness is essential especially for the receiver coil that will be on the vest. In addition to the need of a compact and light receiver coil, a compact battery pack requirement with non-hazardous voltage level to human body is essential.

Dimensions of the transmitter coils that is placed to the charging seat are not as crutial as receiver coil but again performance of it is very critical to have an effective power transfer.

Considering the power transfer distance, charging will be done when the user sits on the charger seat. Therefore, maximum 5-10 cm transfer distance is enough for the selected application.

The analyses presented in this study can be summarized as follows:

i. Advantages and disadvantages of basic compensation methods for IPT

ii. Analytical and numerical calculation of resistance, self-inductance and mutual inductances of planar spiral coils

iii. Analyzing and comparing possible designs by using Pareto-front search

iv. Building and testing two wireless battery charger topologies

v. Performance comparison of passive shielding techniques

Application requirements and design specifications of a wireless power transfer system for a charging vest are not comprehensively studied in the literature. Therefore, determination of the requirements for such applications, their analysis and a design procedure from the beginning to the end are contributions of this thesis to the literature. In addition to these, studying the WPT systems in terms of shielding requirements and effects of shielding on the system performance are the other contributions of this study.

1.2 Thesis Outline

In Chapter 2, several wireless power transfer methods are studied and compared. This chapter also includes design requirements of the charging vest application.

In Chapter 3, four basic compensation topologies for IPT are analytically analyzed. Their advantages and disadvantages over each other are studied. In addition, bifurcation phenomenon is explained and a compensation method is selected within the considerations of advantages and disadvantages.

In Chapter 4, analytical calculations of resistance, self-inductance and mutual inductance for planar spiral coil structure are studied. Obtained results are validated using

ANSYS Maxwell.

In Chapter 5, exact system specitications are determined. A design methodology based on Pareto-front search is applied considering the change in the system efficiency as the distance between coils and operating frequency change. Two different designs are obtained by using outputs of the search and their performances simulated at different load conditions are given.

In Chapter 6, implementation of two different designs are explained. Test setup, procedure and results of different tests are presented. Finally, tests results and loss analysis are discussed.

In Chapter 7, shielding requirements of a typical WPT system are given. Thereafter, effects of different passive shielding methods on a WPT system are discussed. Finally, shielding performances of different shields are analyzed by using ANSYS Maxwell.

In Chapter 8, a general conclusion is made and suggestions for future studies are mentioned.

CHAPTER 2

WIRELESS POWER TRANSFER METHODS AND APPLICATIONS

A general overview of the wireless power transfer (WPT) methods and applications will be given in this chapter to be able to identify the most appropriate method for the charging the battery on a charging vest.

2.1 Wireless Power Transfer Methods

The most commonly used WPT methods are briefly introduced in this section.

Inductive Power Transfer

Inductive power transfer (IPT) is based on magnetically coupled inductors [15]. In such a system, energy is inductively transferred from transmitter to the receiver, where the tranmitter is connected to the source and the receiver is connected to the load. A typical circuit scheme for an inductive power transfer can be seen in Figure 2.1.

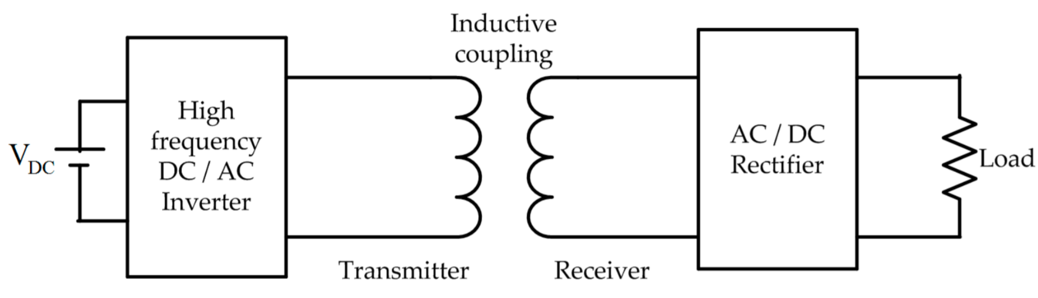

Figure 2.1: A circuit scheme for inductive power transfer [3]

Inductive power transfer method has a very high efficiency when the transmitter and receiver coils are very close to each other that is power transmission distance in range of a few centimeters. Besides the distance between coils, transfer performance in terms of efficiency and transferred power strongly depends on coupling coefficient between two coils, which depends on angular and lateral misalignment between coils. Therefore, IPT is a very popular method for high power transmission systems with a very short power transfer distance [16].

Magnetic Resonance Power Transfer

A big discovery in WPT was the new wireless power transfer scheme based on strong resonant coupling [4]. A strongly coupled coil system is shown in Figure 2.2, where A is the single copper loop connected to the source and B is the single copper loop connected to the load. S and D stand for source and device coils, respectively.

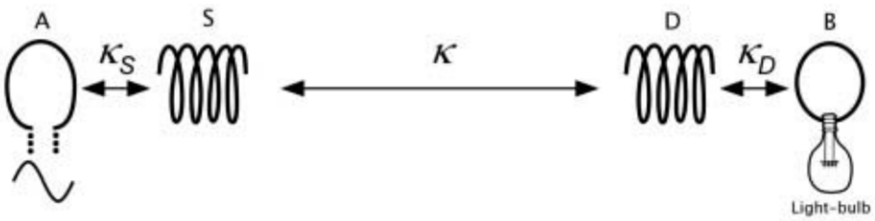

Figure 2.2: Schematic of the strongly coupled coil system [4]

Magnetic resonance power transfer (MRPT) is based on two resonators, S and D as in Figure 2.2, that are tuned at the same resonant frequency and can transfer power effectively over a much longer distance with respect to IPT [16]. With this method, power transfer can be done with either loosely coupled or strongly coupled coils. On the contrary to loosely coupling, strong coupling is not a system with high coupling coefficient but energy coupling is strong with the effect of high quality factor of coils. Here, quality factor of a coil is the ratio between reactive and real power of it. High quality factor enables to compensate the efficiency degredation caused by the low couplings [16]. A more detailed comparison of IPT and MRPT is studied in [17].

Capacitive Power Transfer

A typical structure of a capacitive power transfer (CPT) system is shown in Figure 2.3. Power transfer is realized by transmitter and receiver metal plates. In general, a CPT system uses a high frequency electric field to transfer power. Its main advantages over IPT systems are negligible eddy-current loss, relatively low cost and weight, and better misalignment performance [5]. Transferred power ratings of CPT systems range from a few watts [18] to several kilowatts [19].

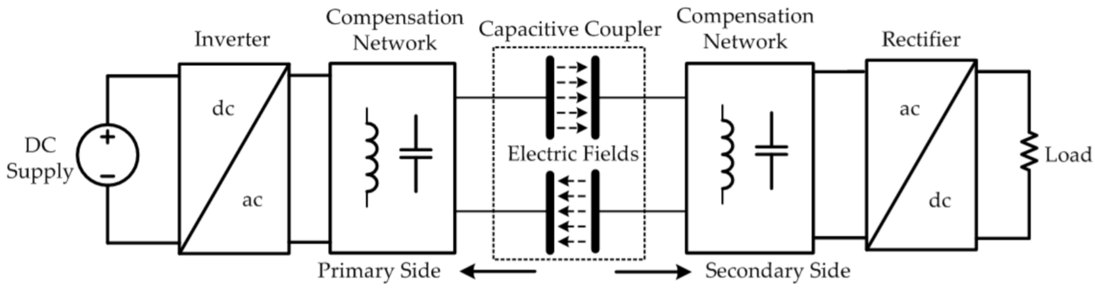

Figure 2.3: Typical structure of a capacitive power transfer system [5]

Radio Frequency Based Power Transfer

Radio frequency (RF) based power transfer method is used for transferring power over very large distances that is in kilometer range. The power is transmitted from an antenna and propagate through the vacuum or air medium in the form of electromagnetic (EM) wave. Because of this propagation, this type of power transfer is called radiative. Since this radiative power emission is omni-directional, overall transfer efficiency is quite low [16].

2.2 Applications

WPT systems offer many advantages over cabled systems. It offers ease of use and better space allocation by eliminating the cables. This is a great advantage for charging the batteries of medical implants. Also, it provides galvanic isolation, so a safer operation is achieved. Another advantage is that, power can be transferred to mobile loads such as electrical vehicles during driving or short stops. Therefore, WPT has many application areas such as home electronics, medical implants and electrical vehicles.

Home Electronics

As most of the home electronics devices are portable, wireless power transfer is quite suitable for this area. As can be seen in Figure 2.4, charging devices like laptops, mobile phones, smart watches and portable music players by using wireless power transfer provides freedom by eliminating cable requirements [6]. Not only for those, using WPT for other devices like quartz clocks reduces battery requirement [20]. One other importance of WPT is for some hazardous plug-and-socket applications, like a blow-dryer in a bathroom. WPT based chargers galvanivally isolate the load, so safety concerns are no longer an issue.

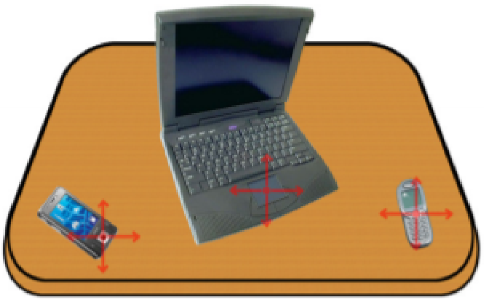

Figure 2.4: An example of wireless charging for home electronics [6]

Medical Implants

Implantable devices play a vital role for human health. They are used to treat dysfunctional organs. Eliminating bulky batteries and extra connection cables of those devices enable having much smaller implantable devices. In addition, requirement for battery replacement by means of a surgery becomes unnecessary with wireless charging. One example for such an application is shown in Figure 2.5.

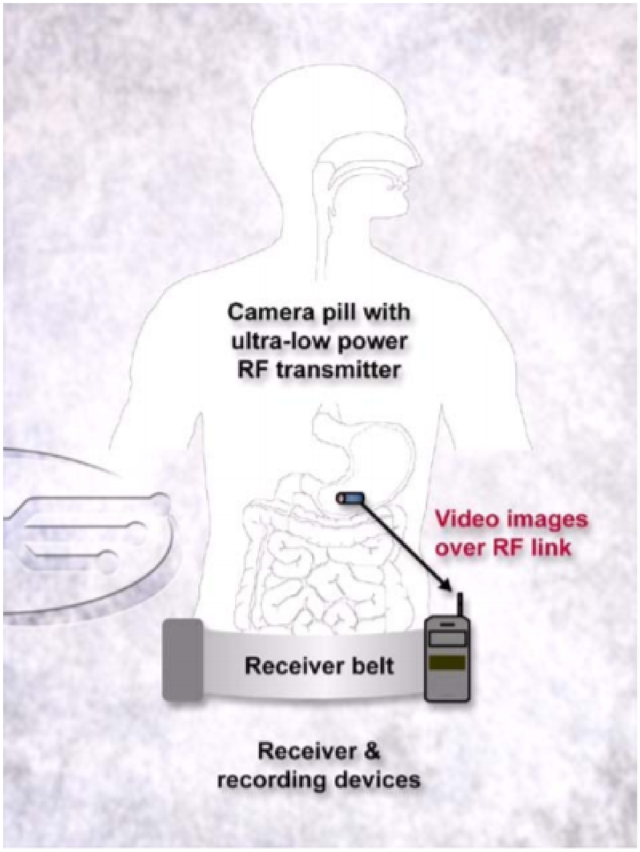

Figure 2.5: Camera pill system with ultra low power transmitter [7]

Electrical Vehicles

Lately, electrical vehicles became more popular than internal-combustion-engine vehicles because of several reasons such as their lower CO_2 emissions. However, range of electrical vehicles are limited due to low energy density of batteries compared to gasoline. Thus, batteries are heavy, bulky and expensive. Moreover, they are made of scarce materials such as lithium, which is also an explosive material [15]. Dynamic wireless charging allows using less batteries and it would improve the performance of the electrical vehicles by lowering their total weight. Also, less battery would lower the severity of explosions in case of an accident. In addition, dynamic charging can reduce waiting time for recharging of the batteries. One example of wireless power transfer for an electrical vehicle is shown in Figure 2.6

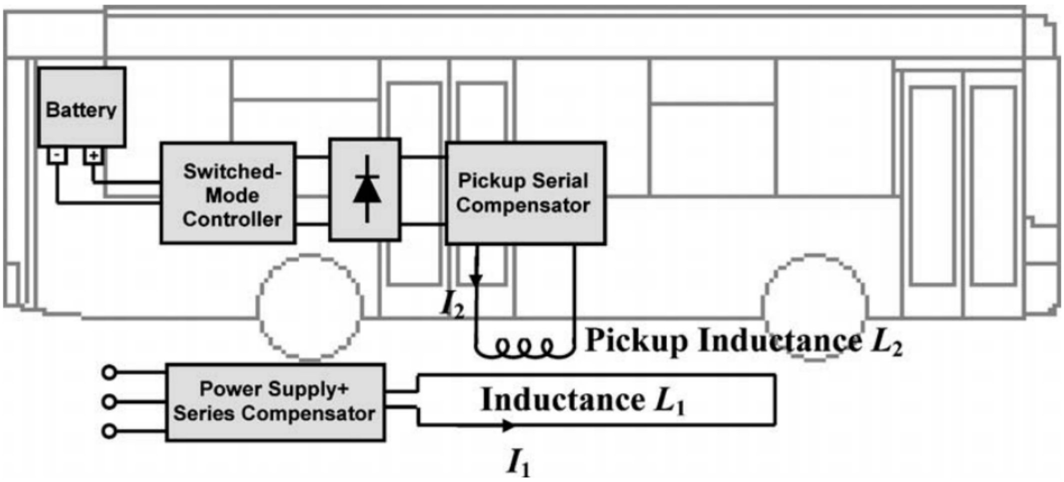

Figure 2.6: Scheme of the inductive power transfer battery charger [8]

2.3 Charging Vest Application Requirements

In addition to the applications that are mentioned, charging the battery on a vest by using WPT can be useful especially for military usage. With this application, when the user sits on the transmitter seat, battery on the user's vest is aimed to be charged with the help of the receiver part that is placed on the back of the vest.

For the receiver side, a compact, flexible and light receiver coil is preferred. The battery that will be charged on the vest is required to be light and compact, too. In addition, voltage level of it must be non-hazardous to human body. For such an application, a Li-ion battery pack that consists of series and parallel connected Li-ion cells would be suitable.

Transmitter side dimension restrictions are not as rigorous as receiver side because transmitter circuit will be placed on the seat. Therefore, both battery pack and transmitter coil don't have to be compact and light. In addition, the battery of vehicle can be used as a power source, instead of an extra battery pack. However, as in the case of receiver side, voltage level of the transmitter battery must also be non-hazardous to human body.

Since battery on the west will be charged while the soldier is sitting, charging distance can be limited to be less than 5-10 cm. Power level of this application is required to be at several tens of watts. Within the knowledge of these requirements, first selection for the design procedure was the power transfer method. In Figure 2.7, different WPT methods are compared in terms of their efficiency as a function of transfer distance. Microwave type, also called as RF, has very low efficiency and it is used for much higher transfer distances. Maximum 5-10 cm transfer distance is covered with induction type and resonance type (MRPT) systems. In addition to those, CPT is not considered in this figure but it is still under consideration. MRPT and CPT requires a very high operating frequency that is in the range of several MHz and above by nature. Because of this requirement, MRPT and CPT are not considered in our design procedure due to the difficulties of high frequency gate driving. Therefore, inductive power transfer (IPT) is selected as the WPT method and it will be analyzed in the next section.

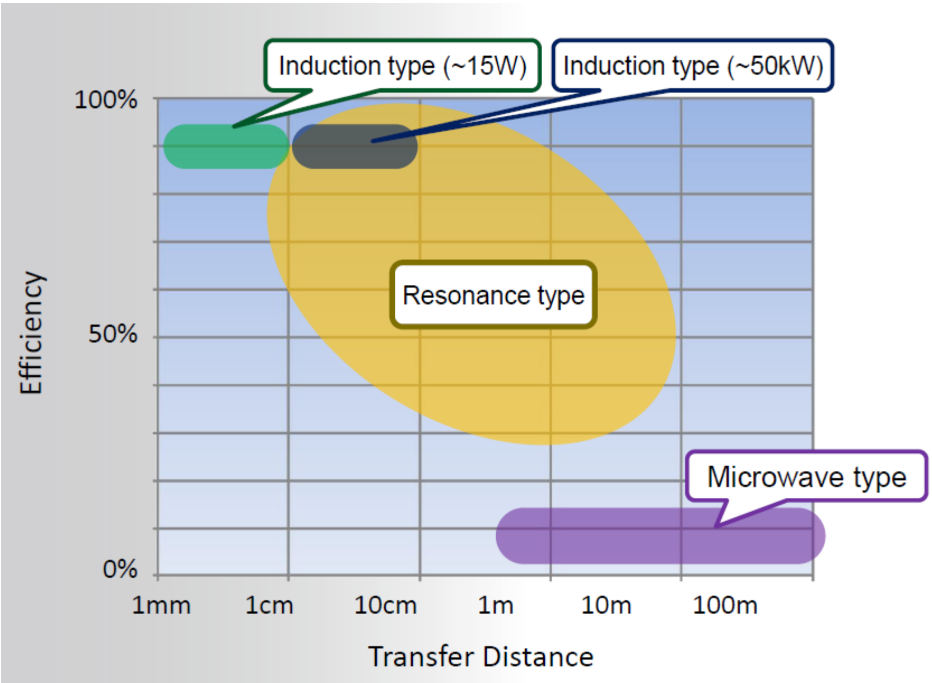

Figure 2.7: Efficiency vs transfer distance regions for different WPT methods [9]

CHAPTER 3

ANALYTICAL INVESTIGATIONS OF INDUCTIVE POWER TRANSFER

Inductive power transfer (IPT) method is found as the most appropriate wireless power transfer method for the target application in the previous chapter. There are several transmitter and receiver topologies that can be used for inductive power transfer. Those will be investigated in detail and their advantages and disadvantages will be compared in this chapter. Finally, a topology will be selected at the end of this chapter after considering all trade-offs.

3.1 Compensation Methods

Equivalent circuit model of a typical IPT system is shown in Figure 3.1. In such a system, magnetic coupling, M, between transmitter (primary) and receiver (secondary) coils is much lower than primary and secondary inductances, L_p and L_s. Thus, effect of leakage inductances of transmitter and receiver coils becomes dominant and load seen by the source is inductive even if a purely resistive load is connected to the secondary, so circulating reactive power exists proportional to the inductive impedance. In order to lower VA rating of the supply and to improve power transfer capability of it, compensation circuits are required [21]. Not only high VA rating requirement of supply but also circulating current leads to extra losses on parasitic resistances. By using proper primary and secondary compensation capacitances, it is possible to eliminate the reactance seen by the source and to make primary voltage and primary current in phase, which called zero phase angle operation (ZPA).

There are basically four compensation topologies that are named as Series-Series (SS), Series-Parallel (SP), Parallel-Series (PS) and Parallel-Parallel (PP), as shown in

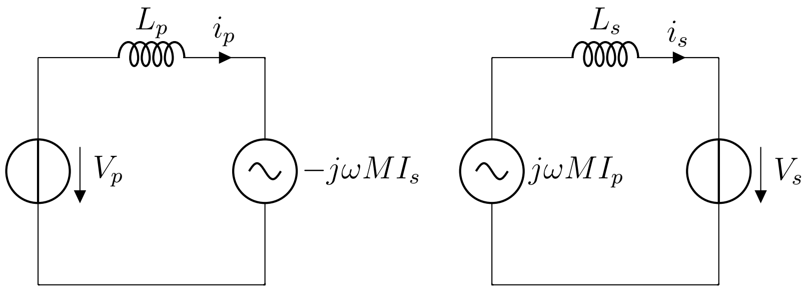

Figure 3.1: Mutual inductance model [10]

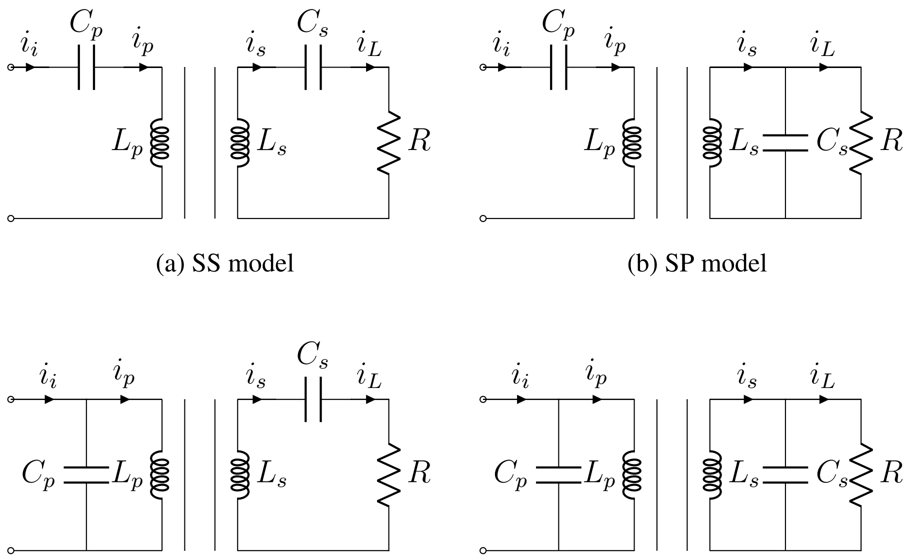

(a) SS model

(b) SP model

(c) PS model

(d) PP model

Figure 3.2: Basic compesation topologies [10]

Figure 3.2. In this figure R stands for the resistance of the resistive load and current subscripts i, p, s and L stands for inverter, primary, secondary and load, respectively. Compensation topologies are named according to the connection of the compensation capacitors, C_p and C_s.

There exist many different methods in the literature in order to analyze IPT models with compensation circuits such as coupled mode theory and circuit theory [17]. In the following subsections, the 4 compensation circuits that are SS, SP, PS and PP are investigated by using circuit theory. In addition to the the circuit components shown in Figure 3.2, series resistances of the transmitter coil, R_p, and the receiver coil, R_s, which are not shown in Figure 3.2 for the sake of simplicity, will be taken into account.

Starting point of the analytical process is to reflect secondary side impedance to the primary side. Following expression is the relation of the secondary side impedance and reflected form of it to the transmitter, Z_r [21].

$$Z_r = \frac{\omega^2 M^2}{Z_s} \tag{3.1}$$

Where M is mutual inductance, ω is the operating frequency and Z_s is the secondary side impedance. Coupling coefficient that depends on mutual inductance, transmitter and receiver self inductance can be expressed as:

$$k = \frac{M}{\sqrt{L_p L_s}} \tag{3.2}$$

The relation between primary and secondary currents is as follows [21]:

$$I_p = \frac{Z_s I_s}{j\omega M} \tag{3.3}$$

Where resonant frequency ω_0 is:

$$\omega_0 = \frac{1}{\sqrt{C_s L_s}} = \frac{1}{\sqrt{C_p L_p}} \tag{3.4}$$

In order to find transferred power, P_{tr}, and output power, P_{out}, following relations can be used:

$$P_{tr} = Re\{Z_r\} {I_p}^2 \tag{3.5}$$

$$P_{out} = R{I_L}^2 \tag{3.6}$$

Rest of the analysis are specific to the compensation types, thus analyzed individually.

3.1.1 Series-Compensated Secondary

A series-compensated secondary topology can be seen in Figures 3.2a and 3.2c. Impedance of a series-compensated secondary can be written as:

$$Z_s = j\omega L_s + \frac{1}{j\omega C_s} + R_s + R \tag{3.7}$$

By using (3.1) and (3.7), reflected form of the secondary side impedance to the primary side has the following form.

$$Z_r = \frac{\omega^2 M^2}{R_s + R + j(\omega L_s - \dfrac{1}{\omega C_2})} \tag{3.8}$$

So, at $\omega = \omega_0$, reflected impedance to the primary side is pure resistive.

One of the advantages of the series-compensated secondary is that no reactance is reflected to the primary side when operating at resonant frequency. Therefore, the variation of coupling between transmitter and receiver coils doesn't affect primary resonant capacitor size. When a typical IPT system is considered, perfect alignment of transmitter and receiver coils is impossible. Therefore, this advantage cannot be underestimated. Variation need of primary resonant capacitance with varying load and varying coupling coefficient will be mentioned in the latter subsections.

In addition, load current is the same as the secondary coil current. This eases transferred power and output power calculations.

$$I_L = I_s \tag{3.9}$$

Finally, transferred power and output power calculation is shown below. Primary current calculation will be mentioned in the latter subsections.

$$P_{tr} = Re\{Z_r\}{I_p}^2 = (R_s + R)(\frac{j\omega M I_p}{Z_s})^2 \tag{3.10}$$

$$P_{out} = R(\frac{j\omega M I_p}{Z_s})^2 \tag{3.11}$$

3.1.2 Parallel-Compensated Secondary

A parallel-compensated secondary topology is shown in Figures 3.2b and 3.2d. Impedance of a parallel-compensated secondary can be written as:

$$Z_s = j\omega L_s + R_s + \frac{R}{1 + j\omega C_s R} \tag{3.12}$$

Reflected form of the secondary side impedance to the primary side is expressed as below:

$$Z_r = \frac{\omega^2 M^2}{j\omega L_s + R_s + \dfrac{R}{1 + j\omega C_s R}} \tag{3.13}$$

On the contrary to the series-compensated secondary, it can easily be seen in (3.13) that imaginary part of the reflected impedance is not zero even if at the resonance frequency operation. Thus, primary resonant capacitor should be determined according to the coupling factor, M, in order to operate in ZPA. This is the main disadvantage of parallel compensated secondary topology over series compensated secondary case.

In this case, load current is not equal to secondary coil current as can be seen in (3.14). Therefore, calculation of the transferred power and the output power is not as trivial as in series-compensated secondary case.

$$I_L = \frac{I_s}{1 + j\omega C_s R} \tag{3.14}$$

Output power expression is shown below. Required primary current in order to calculate output power will be analyzed in the following subsections.

$$P_{out} = R(\frac{j\omega M I_p}{Z_s}\frac{1}{1 + j\omega C_s R})^2 \tag{3.15}$$

One advantage of the parallel-compensated secondary is that only ripple current flows through the resonant capacitor in parallel-compensated case where the total load current flows through the resonant capacitor in series-compensated secondary case. Thus, current carrying capability of resonant capacitor of series-compensated secondary must be much higher than that of parallel-compensated secondary.

3.1.3 Series-Compensated Primary

A series-compensated primary topology can be seen in Figures 3.2a and 3.2b. Series-compensated primary circuit can be driven by a voltage source where parallel compensated primary circuit can be driven by a current source. Since it is driven by a voltage source, a half bridge or a full bridge switching circuit can be used for this purpose. As in the case of series-compensated secondary, capacitors with a high current carrying capability are required in this case. In addition, primary coil current is equal to the inverter current, so power equations can easily be solved.

Load impedance expression seen by the source can be seen in the expression below [21].

$$Z_{in} = j(\omega L_p - \frac{1}{\omega C_p}) + R_p + Z_r \tag{3.16}$$

As can be concluded from (3.16), the most important disadvantage of a series compensated primary is that existing of a secondary coil is a must. In the absence of a secondary, load seen by the source at resonant frequency is limited by the resistance of the primary coil, R_p. Therefore, an extra effort is needed to assure a safe operation.

The relationship between inverter current and primary voltage is as below:

$$I_i = I_p = \frac{V_i}{j(\omega L_p - \frac{1}{\omega C_p}) + R_p + Z_r} \tag{3.17}$$

3.1.4 Parallel-Compesated Primary

A parallel-compensated primary topology can be seen in Figures 3.2c and 3.2d. Current carrying capability of the resonant capacitor doesn't have to be as high as in the series-compensated primary case.

Load impedance seen by the source can be expressed as:

$$Z_{in} = \frac{1}{\dfrac{1}{j\omega L_p + R_p + Z_r} + j\omega C_p} \tag{3.18}$$

One of the advantages of this topology over a series-compensated primary is that operation is completely safe when there is no receiver coil. Because in this case, impedance seen by the source goes to infinity as seen in (3.18). Besides, dependency of the primary resonant capacitor to the load and coupling factor can be counted as an important disadvantage. Therefore, in order to ensure ZPA operation, variable capacitor banks are needed.

Inverter current and source voltage relations can be deriven as below.

$$I_i = \frac{V_i}{\dfrac{1}{\dfrac{1}{j\omega L_p + R_p + Z_r} + j\omega C_p}} \tag{3.19}$$

Primary coil current and inverter current relation is shown below.

$$I_p = I_i - j\omega C_p V_p \tag{3.20}$$

Finally, electrical quantities of the four basic topologies are listed in Table 3.1

Table 3.1: Electrical quantities for the four basic topologies [1]

	SS	SP	PS	PP
$\vec{I}_p$	$\vec{I}_i$	$\vec{I}_i$	$\vec{I}_i - j\omega C_p \vec{V}_i$	$\vec{I}_i - j\omega C_p \vec{V}_i$
$\vec{I}_{Cp}$	$\vec{I}_p$	$\vec{I}_p$	$j\omega C_p \vec{V}_i$	$j\omega C_p \vec{V}_i$
$\vec{V}_{Cp}$	$\frac{\vec{I}_i}{j\omega C_p}$	$\frac{\vec{I}_i}{j\omega C_p}$	$\vec{V}_i$	$\vec{V}_i$
$\vec{I}_s$	$\frac{j\omega M \vec{I}_p}{R_s + R + j(\omega L_s - \frac{1}{\omega C_s})}$	$\frac{j\omega M(1 + j\omega C_s R)\vec{I}_p}{R + (R_s + j\omega L_s)(1 + j\omega C_s R)}$	$\frac{j\omega M \vec{I}_p}{R_s + R + j(\omega L_s - \frac{1}{\omega C_s})}$	$\frac{j\omega M(1 + j\omega C_s R)\vec{I}_p}{R + (R_s + j\omega L_s)(1 + j\omega C_s R)}$
$\vec{I}_L$	$\vec{I}_s$	$\frac{\vec{I}_s}{1 + j\omega C_s R}$	$\vec{I}_s$	$\frac{\vec{I}_s}{1 + j\omega C_s R}$
$\vec{I}_{Cs}$	$\vec{I}_s$	$j\omega C_s R \vec{I}_L$	$\vec{I}_s$	$j\omega C_s R \vec{I}_L$
$\vec{V}_{Cs}$	$\frac{\vec{I}_s}{j\omega C_s}$	$\frac{\vec{I}_{Cs}}{j\omega C_s}$	$\frac{\vec{I}_s}{j\omega C_s}$	$\frac{\vec{I}_{Cs}}{j\omega C_s}$
$\vec{V}_L$	$R\vec{I}_L$	$\vec{I}_{Cs}$	$R\vec{I}_L$	$\vec{I}_{Cs}$

3.2 Variation of Primary Compensation Capacitor

In SP, PP, PS topologies, there exists reactance of the reflected impedance of the secondary, even if the operation frequency is at the resonant frequency of the primary and secondary sides. So, operation at resonance frequency doesn't always mean ZPA operation. Therefore, in order to calculate primary compensation capacitor, (3.4) is not enough and mutual inductance and load resistance in some cases are required. Required primary capacitance relations are listed in Table 3.2.

Table 3.2: Primary capacitance for ZPA operation [2]

Topology	Primary capacitance C_p
SS	$\dfrac{L_s C_s}{L_p}$
SP	$\dfrac{{L_s}^2 C_s}{(L_p L_s - M^2)}$
PS	$\dfrac{L_p}{(\dfrac{M^2}{L_s C_s R})^2 + \dfrac{{L_p}^2}{L_s C_s}}$
PP	$\dfrac{(L_p L_s - M^2){L_s}^2 C_s}{M^4 R^2 C_s + L_s (L_p L_s - M^2)^2}$

In order to generalize the required compensation capacitance, calculation of normalized primary capacitance, C_{pn}, can be defined as in (3.21), the ratio between the primary capacitance in Table 3.2 and calculated value by using the definition of resonance frequency, as in (3.4).

$$C_{pn} = \frac{C_p}{\frac{C_s L_s}{L_p}} \tag{3.21}$$

Required normalized primary capacitance values for ZPA operation are visualized in Figure 3.3 as a function of coupling coefficient. In SS topology, primary compensation capacitance does not depend on coupling coefficient and load. In SP topology, primary capacitance only depends on magnetic coupling constant, k, and required capacitance increases as k increases. For PS and PP topologies, primary capacitance depends both on magnetic coupling constant and load, hence required primary capacitance varies as a function of coupling constant.

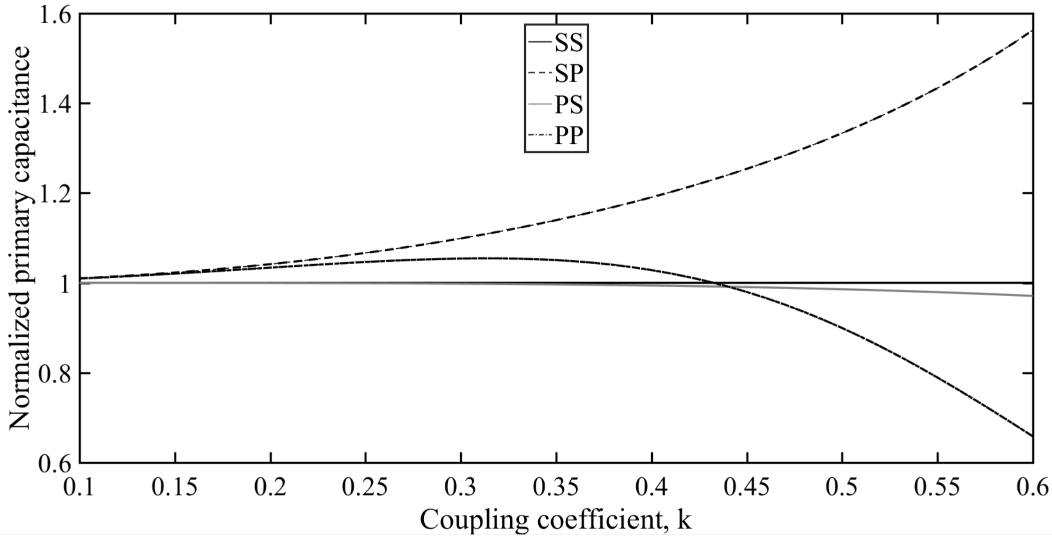

Figure 3.3: Primary compensation vs coupling coefficient

3.3 Effect of Magnetic Coupling Variation

In order to observe the effect of the magnetic coupling variation to the system behaviour, a pair of coils is selected. Corresponding mutual inductance variation with respect to misalignment percentage is shown in Figure 3.4, where the misalignment percentage is set to 50%, when the center of the receiver coil is aligned with the last turn of transmitter coil.

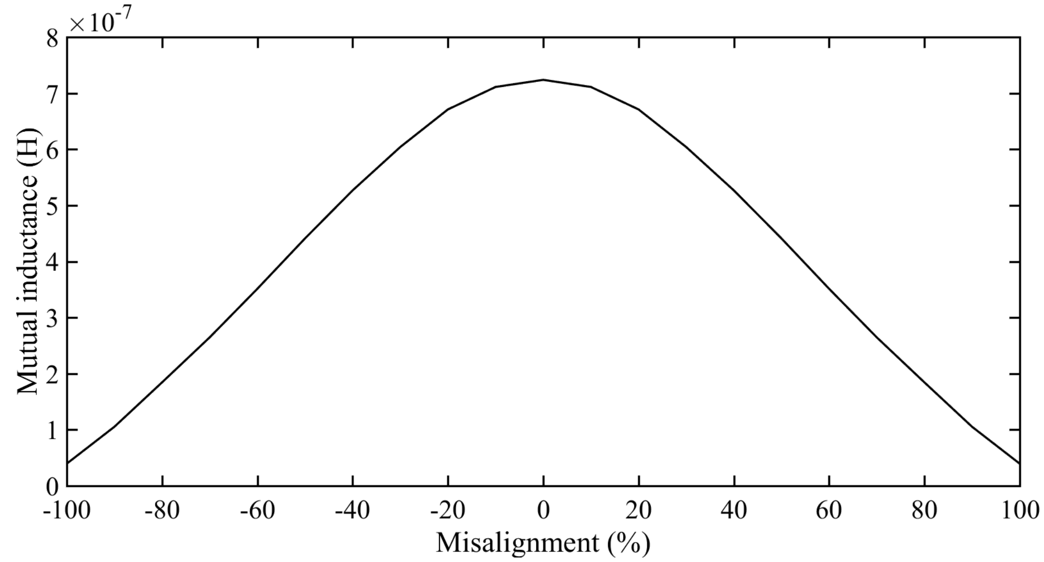

Figure 3.4: Mutual inductance vs misalignment

Total impedance seen by the source, Z_t, with respect to the misalignment is shown in Figure 3.5, where Z_{t0} is the impedance when the misalignment is at 0%. In this figure, SS and SP curves are overlapped. As mentioned earlier, it is seen that total impedance increases in parallel-compensated primary circuits with misalignment. On the other hand, total impedance seen by the source decreases in series-compensated primary circuits [22].

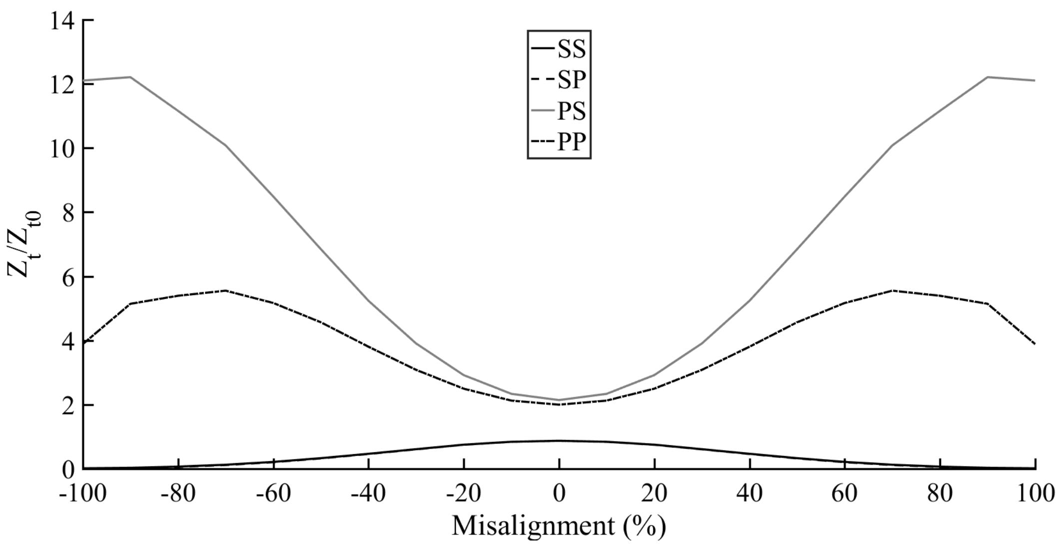

Figure 3.5: Total impedance seen by the source vs misalignment

By using the impedance variation, primary current variation in Figure 3.6 can be obtained. As expected, primary current, I_i increases dramatically in series-compensated primary circuits where it decreases in parallel-compensated primary circuits. In this figure, I_{i0} is the current when the misalignment is at 0%.

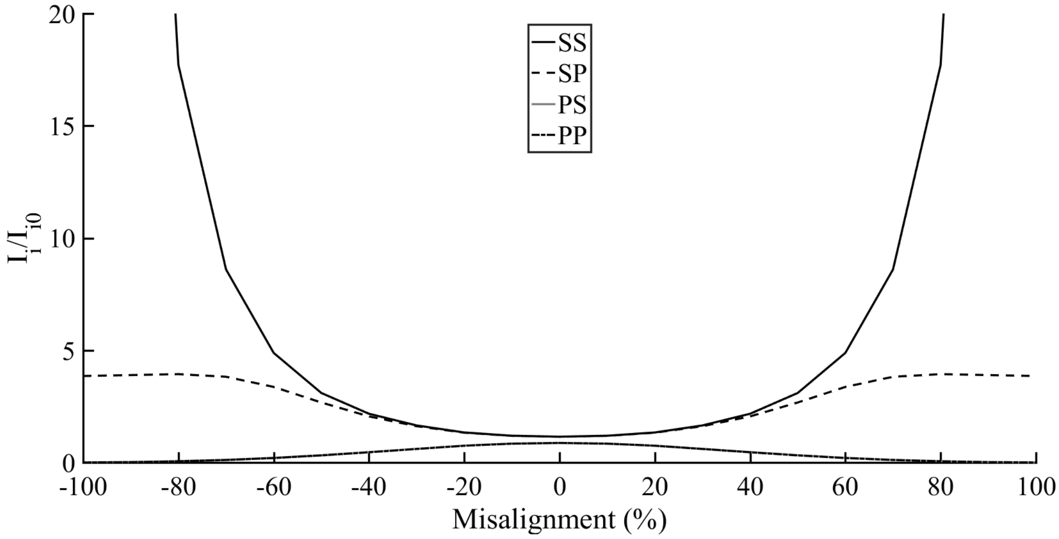

Figure 3.6: Source current vs misalignment

3.4 Bifurcation Phenomena

In order to operate at ZPA, operating frequency should be at resonance frequency. However, as the loading and quality factor of receiver changes, extra ZPA frequencies arise. This phenomenon is called "bifurcation" [10]. In order to study bifurcation phenomenon, first, real and imaginary parts of the reflected impedance of the receiver side should be determined as follows [10]:

$$Re\{Z_r\} = \begin{cases} \dfrac{\omega^4 {C_s}^2 M^2 R}{(\omega^2 C_s L_s - 1)^2 + \omega^2 {C_s}^2 R^2}, & \text{series compensated secondary} \\ \dfrac{\omega^2 M^2 R}{R^2(\omega^2 C_s L_s - 1)^2 + \omega^2 {L_s}^2}, & \text{parallel compensated secondary} \end{cases} \tag{3.22}$$

and

$$Im\{Z_r\} = \begin{cases} \dfrac{-\omega^3 C_s M^2(\omega^2 C_s L_s - 1)}{(\omega^2 C_s L_s - 1)^2 + \omega^2 {C_s}^2 R^2}, & \text{series compensated secondary} \\ \dfrac{-\omega^3 M^2(C_s R^2(\omega^2 C_s L_s - 1) + L_s)}{R^2(\omega^2 C_s L_s - 1)^2 + \omega^2 {L_s}^2}, & \text{parallel compensated secondary} \end{cases} \tag{3.23}$$

Parasitic resistances of primary and secondary coils are neglected for the sake of simplicity in the two expressions above. After this point, calculations will be done only for the SS topology. Normalized frequency with respect to resonance frequency, u, and normalized reflected impedance, Z_n, with respect to reflected impedance at resonance frequency, Z_{r0}, are defined as:

$$u = \frac{\omega}{\omega_0} \tag{3.24}$$

and

$$Z_n = \frac{Z_t}{Re\{Z_{r0}\}} = \frac{Re\{Z_t\}}{Re\{Z_{r0}\}} + j\frac{Im\{Z_t\}}{Re\{Z_{r0}\}} = Re\{Z_n\} + jIm\{Z_n\} \tag{3.25}$$

$$\frac{Re\{Z_r\}}{Re\{Z_{r0}\}} = \frac{u^4}{(u^2-1)^2 {Q_s}^2 + u^2} \tag{3.26}$$

and

$$\frac{Im\{Z_r\}}{Re\{Z_{r0}\}} = -\frac{u^3(u^2-1)Q_s}{(u^2-1)^2 {Q_s}^2 + u^2} \tag{3.27}$$

where quality factors Q_p and Q_s are:

$$Q_p = \frac{R}{{\omega_0}^3 C_s M^2} \tag{3.28}$$

and

$$Q_s = \frac{\omega_0 L_s}{R} \tag{3.29}$$

$$Im\{Z_n\} = \frac{(u^2-1)((Q_pQ_s{}^2 - Q_s)u^4 + (Q_p - 2Q_pQ_s{}^2)u^2 + Q_pQ_s{}^2}{u(u_2-1)^2Q_s{}^2 + u^3} \tag{3.30}$$

As seen in (3.30), nominator of $Im\{Z_n\}$ is a biquadratic polynomial. In such a polynomial, its generalized discriminant is as follows:

$$\Delta = a_2^2 - 4a_4a_0 \tag{3.31}$$

For SS topology case, discriminant of the nominator with respect to quality factor of primary and secondary can be written as:

$$\Delta = Q_p[Q_p(1-4Q_s^2) + 4Q_s^3] \tag{3.32}$$

Multiple roots exist for any biquadratic polynomial if its discriminant is less than zero. Therefore, required condition for the bifurcation operation for SS topology is shown in below.

$$Q_p < \frac{4Q_s^3}{4Q_s^2 - 1} \tag{3.33}$$

As seen in the Figure 3.7, reflected imaginary impedance intersect with the x axis at 3 different points for small Q_p values. In this case, Q_s is taken as 10.

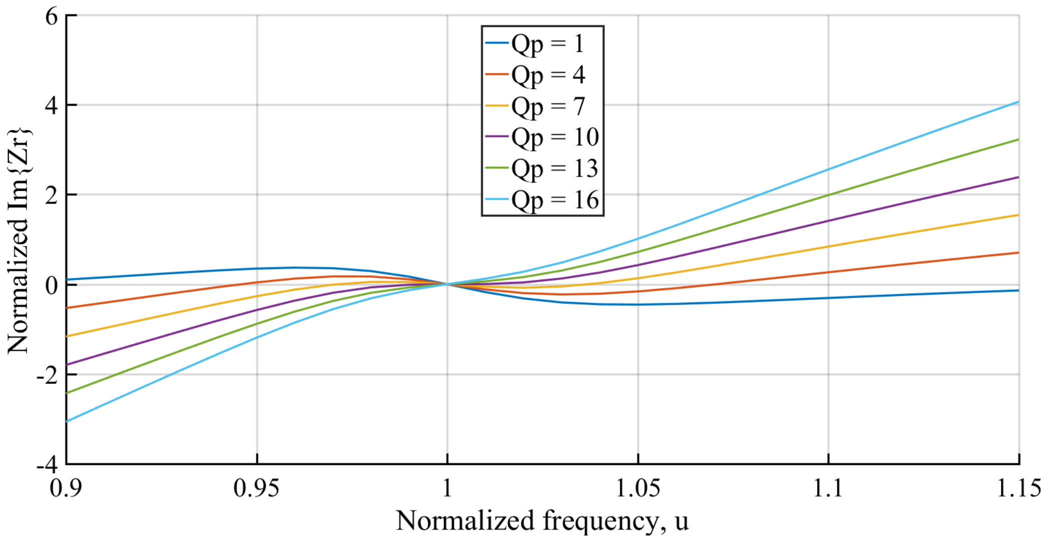

Figure 3.7: Normalized reflected imaginary impedance vs normalized frequency

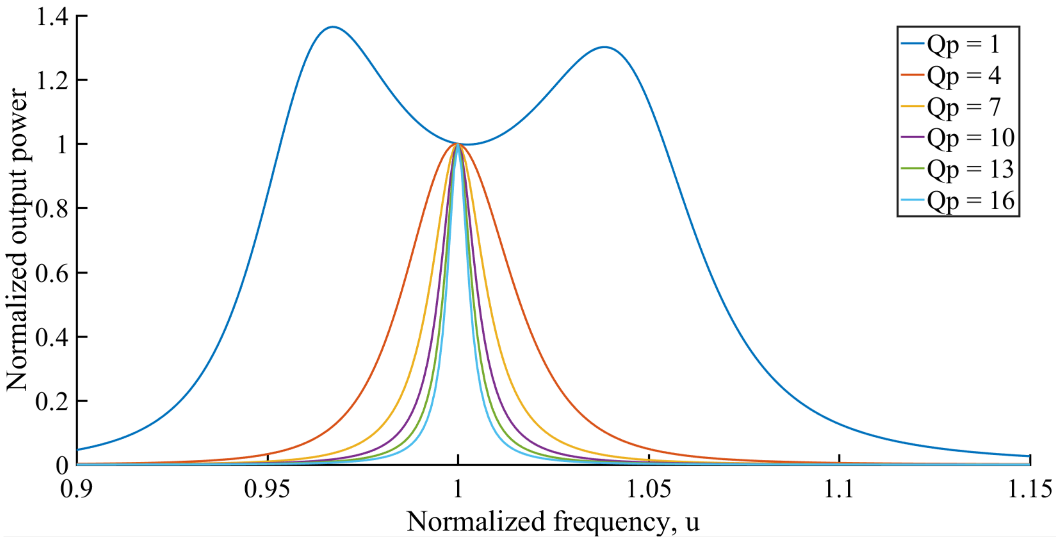

Figure 3.8: Normalized output power vs normalized frequency

Effect of bifurcation to the output power of the system is shown in Figure 3.8. As the Q_p gets much smaller than the Q_s, output power increases as the operating frequency diverges from the resonant frequency until it reaches to other ZPA points. If bifurcation operation is the desired operation, care must be taken while designing controller, because in bifurcation operation, transferred output power behaviour is not as predictable as in normal operation.

3.5 Discussion

In this chapter, requirement for compensation is mentioned. Basic compensation topologies are studied analytically and their trade-offs were discussed. Finally, bifurcation phenomenon is explained.

After all these trade-offs, SS compensation is selected, because of that it does not require compensation capacitor variation in order to operate in ZPA and its design parameters are easy to calculate analytically. Moreover, it can be driven by a basic voltage source circuit, such as a half bridge or a full bridge.

CHAPTER 4

PLANAR SPIRAL COIL ANALYSIS

After selecting IPT as the wireless power transfer method and SS topology as the compensation type, next step is to select a coil configuration. Since planar spiral coils are used in most of the WPT applications due to their compact design [23], this structure shown in Figure 4.1 is selected in this thesis as well. Not only for its compact design, analytical calculation ease of it was another reason of planar spiral coil structure selection.

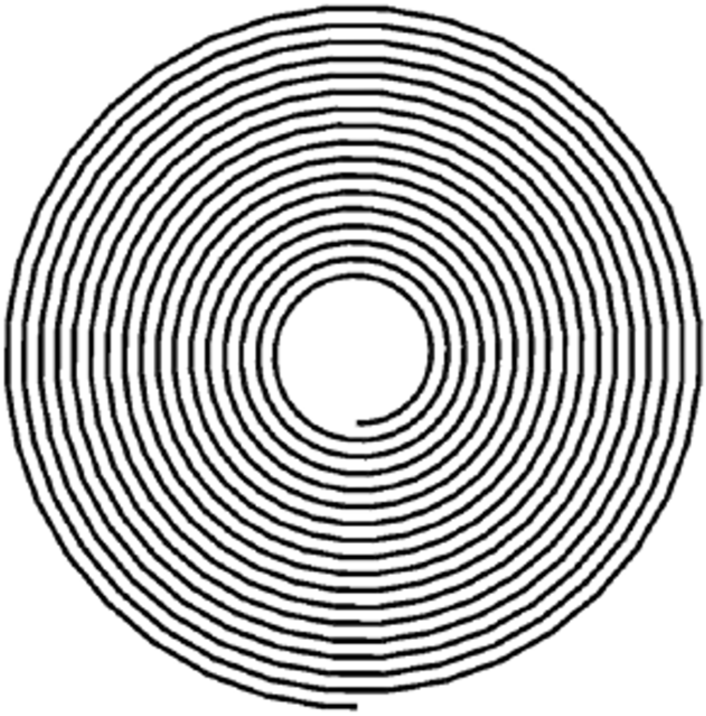

Figure 4.1: Planar spiral coil

In order to design a proper wireless battery charger, coil parameters are required. For this purpose, analytical calculation of resistance, self inductance and mutual inductance is studied in this chapter.

4.1 Resistance Calculation

Calculating resistance of coils is one of the fundamental requirements while designing coils. In general, IPT designs are mostly operated at frequencies ranging from a few kilohertz to hundred of megahertz depending on the application [24]. Since the operating frequency is high, skin effect must be taken into account. Using Litz wire is the most popular solution to lower the increase in resistance due to skin effect. Thus, Litz wire is selected for both transmitter and receiver coils. In addition to skin effect, additional factors that effect resistance of a Litz wire exist. In the following subsections, those effects will be studied.

4.1.1 Resistance of a Litz Wire

An ideal structure of a Litz wire is shown in Figure 4.2. A Litz wire has n_0 number of isolated and twisted strands. Ideally, each strand takes all strand positions in the length of λ_c as shown in Figure 4.2. With this transposition, each strand has the same resistance, therefore a uniform current density can be achieved.

The total power loss of a Litz wire has three different components [11]. First loss component is the conduction loss, P_{cond}. Conduction loss is related with the current in the strand including skin effect. Second loss component is due to the eddy current in each strand induced by other strands, named as P_{ind_int}. Final loss component is caused by the eddy current in the whole bundle due to the other windings, called as external induced power loss, P_{ind_ext}. Total power loss can be expressed as a function of resistances representing each loss mechanism as below [11]:

$$P_T = P_{cond} + P_{ind\_int} + P_{ind\_ext} \tag{4.1}$$

$$P_T = (R_{cond} + R_{ind\_int} + R_{ind\_ext}) I^2/2 \tag{4.2}$$

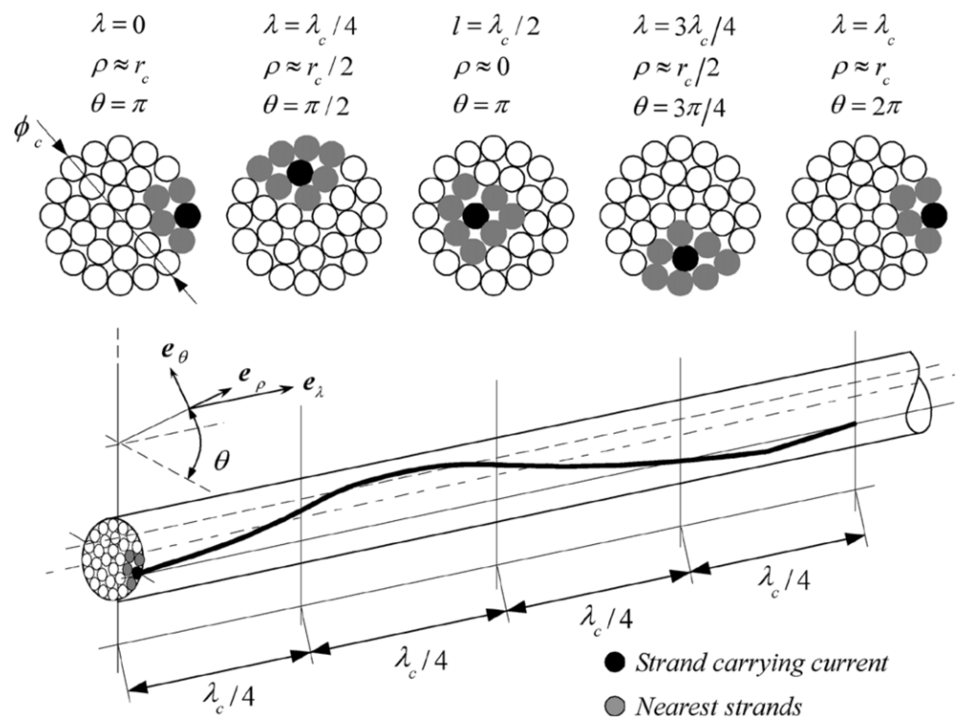

Figure 4.2: An ideal Litz wire structure [11]

Conduction Resistance

Conduction resistance is basically frequency dependent resistance of a wire with n_0 number of strands. Resistance per unit length of a Litz wire can be expressed as [25]:

$$R_{cond\_u.l.} = \frac{1}{n_0}\frac{\xi}{2\pi r_0 \sigma}\Phi_{cond}(\xi r_0) \qquad \Omega/m \tag{4.3}$$

where

$$\Phi_{cond}(\xi r_0) = \frac{ber(\xi r_0)bei'(\xi r_0) - ber'(\xi r_0)bei(\xi r_0)}{ber'^2(\xi r_0) + bei'^2(\xi r_0)} \tag{4.4}$$

$$\xi = \sqrt{\mu\sigma\omega} = \frac{\sqrt{2}}{\delta} \tag{4.5}$$

where δ is skin depth, μ is permeability, σ is the conductivity of the conductor, r_0 is the radius of a strand and $ber,\ bei,\ ber'$ and bei' are Kelvin functions [26].

Internal Induction Resistance

Second power loss component of a Litz wire is due to internal induction loss. Current in each strand disturbs current uniformity in a target strand via eddy current induction. Resistance per unit length arisen from internal induction expression is as in (4.6) and it is studied in detail in [11].

$$R_{ind\_int\_u.l.} = n_0 \frac{-\xi r_0 \Phi_{ind}}{3\pi r_c^2 \sigma} \tag{4.6}$$

where r_c is the radius of the bundle and Φ_{ind} is:

$$\Phi_{ind} = \frac{[ber_2(\xi r_0)ber'(\xi r_0) + [bei_2(\xi r_0)bei'(\xi r_0)]}{ber^2(\xi r_0) + bei^2(\xi r_0)} \tag{4.7}$$

Again ber_2 and bei_2 functions are Kelvin functions [26].

External Induction Resistance

Previously given resistance expressions allow us to calculate a straight Litz wire's frequency dependent resistance. For a planar spiral coil with N number of turns, induced H-field in a turn by other turns disturbs uniformity of the current distribution, so it influences the resistance of the turn. Therefore, current distribution is no longer rotationally symmetrical and an extra resistance component, R_{ind_ext}, arises [25]:

$$R_{ind\_ext} = n_0 \frac{-2\pi^2 \xi r_o \Phi_{ind}}{\sigma} \sum_{i=1}^{N} [a_i < H_{o,i}^2 >] \tag{4.8}$$

Where $< H_{o,i}^2 >$ is the H-field induced in the i-th turn and a_i is the radius of the i-th turn.

As seen in (4.8), in order to find resistance due to proximity effect, H-field that affects current distribution must be calculated. Since in an ideal Litz wire, current is expected to be equally distributed, Litz wire bundle can be taken as a single turn as in Figure 4.3 while calculating H field. Based on this assumption, the analysis procedure proposed in [27] can be followed. In Figure 4.3, the target wire is named as A and the other wires that affects the target wire's current distribution are named as B and C. Each wire's radius is r_0 and each wire is excited by I_0 Amps in x-direction. Z-directed H-fields generated by left and right wires as a function angle θ is as follows:

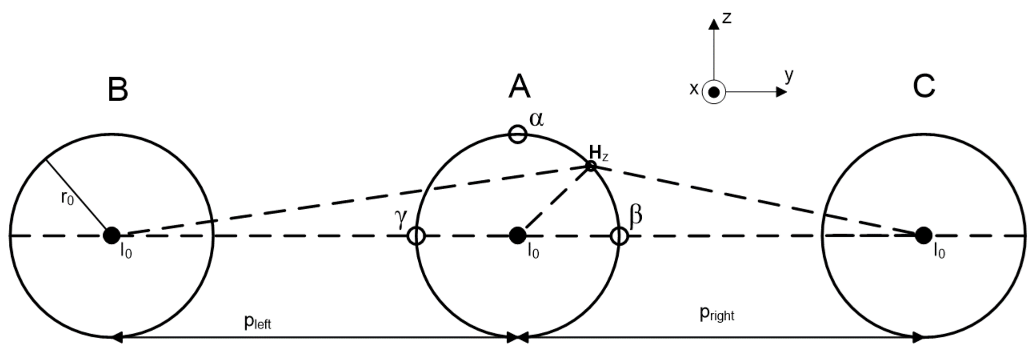

Figure 4.3: H-field on target wire A

$$\vec{H}_{z,right} = -\vec{z}\frac{I_0}{2\pi}\frac{p_{right} - r_0 cos\theta}{{p_{right}}^2 + {r_0}^2 - 2p_{right}r_0 cos\theta} \tag{4.9}$$

$$\vec{H}_{z,left} = \vec{z}\frac{I_0}{2\pi}\frac{p_{left} + r_0 cos\theta}{{p_{left}}^2 + {r_0}^2 + 2p_{left}r_0 cos\theta} \tag{4.10}$$

By selecting 3 points, which are $\alpha_{@\theta=90^0}$, $\beta_{@\theta=0^0}$ and $\gamma_{@\theta=180^0}$, total H-fields can be approximated as below:

$$H_{\alpha,left} = \frac{I_0}{2\pi}\frac{p_{left}}{p_{left}{}^2 + r_0{}^2} \tag{4.11}$$

$$H_{\alpha,right} = \frac{I_0}{2\pi}\frac{p_{right}}{p_{right}{}^2 + r_0{}^2} \tag{4.12}$$

$$H_\beta = H_{\beta,left} - H_{\beta,right} = \frac{I_0}{2\pi}(\frac{1}{p_{left} + r_0} - \frac{1}{p_{right} - r_0}) \tag{4.13}$$

$$H_\gamma = H_{\gamma,left} - H_{\gamma,right} = \frac{I_0}{2\pi}(\frac{1}{p_{left} - r_0} - \frac{1}{p_{right} + r_0}) \tag{4.14}$$

(4.15)

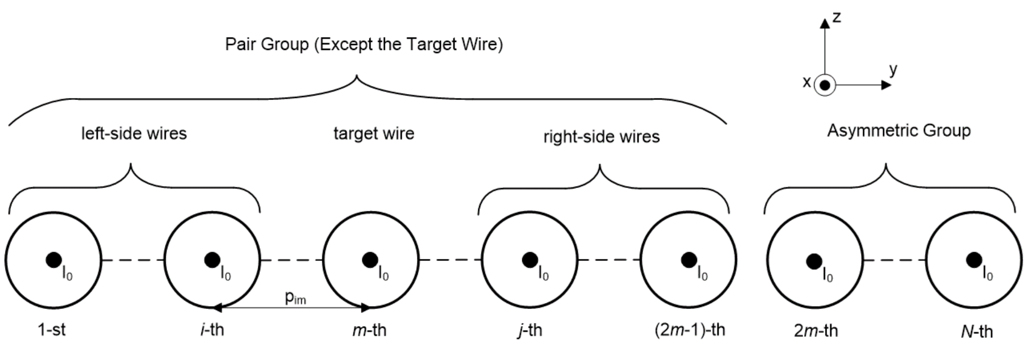

Figure 4.4: Target wire "m" and other effective groups

This approach can be also extended to N number of turns by grouping the turns into pair and asymmetric groups. In Figure 4.4, N number of wires each with r_0 radius and I_0 current, are shown. H-field will be calculated on the target wire, m, and effective wires of H-field on the target wire are grouped as "pair group" and "asymmetric group". Pair group consist of the wires that a left-side wire corresponds to a right-side wire. Asymmetric group is the all the remaining wires [27]. Pair group has influence on the points β and γ and asymmetric group has influence on the reference point, α. At the end, total H-field on the target wire can be calculated as the vectorel sum of $H_{m,pair}$ and $H_{m,asy}$.

$$\vec{H}_m = \vec{H}_{m,pair} + \vec{H}_{m,asy} = \vec{z}H_m \tag{4.16}$$

H-fields generated by the pair group and the asymmetrical group is as follows:

$$\vec{H}_{pair} = \vec{z}H_{pair} = \vec{z}\sqrt{\frac{1}{2}({H_\beta}^2 + {H_\gamma}^2)} \tag{4.17}$$

H-field applied to the target wire, m, from the pair group is expressed as follows. In this expression, i^{th} and j^{th} wires are the ones with the same distance to target wire. Therefore, the relationship between i, j and m is $i + j = 2m$.

$$H_{m,pair} = \begin{cases} 0, & for\ m = 1\ and\ N \\ \sum_{i=1}^{m-1} H_{m,pair}(i,j), & for\ 1 <\ m \leq [N/2] \\ \sum_{i=2m-N}^{m-1} H_{m,pair}(i,j), & for\ [N/2] < m < N \end{cases} \tag{4.18}$$

These expressions can be summarized in the expression below.

$$\vec{H}_{m,pair} = \vec{z}H_{m,pair}(i,j) \tag{4.19}$$

$$\vec{H}_{m,pair} = -\vec{z}\frac{I_0}{2\pi}\sqrt{\frac{{p_{im}}^2 + {r_0}^2}{({p_{im}}^2 - {r_0}^2)^2} + \frac{{p_{mj}}^2 + {r_0}^2}{({p_{mj}}^2 - {r_0}^2)^2} - \frac{2(p_{im}p_{mj} - {r_0}^2)}{({p_{im}}^2 - {r_0}^2)({p_{mj}}^2 - {r_0}^2)}} \tag{4.20}$$

Second component of the total H-field applied to the target wire is applied by asymmetric group. In the following expression, H-field applied to the target wire, m, from k^{th} asymmetric wire is shown.

$$\vec{H}_{m,asy}(k) = \vec{z}H_{m,asy}(k) = -\vec{z}\frac{I_0}{2\pi}\frac{p_{mk}}{{p_{mk}}^2 + {r_0}^2} \tag{4.21}$$

Total asymmetric H-field applied to the target wire, m, can be calculated as follows:

$$H_{m,asy} = \begin{cases} 0, & for\ m = N/2 \\ \sum_{k=2m}^{N} H_{m,asy}(k), & for\ 1 \leq m \leq [N/2] \\ \sum_{k=1}^{2m-N-1} H_{m,asy}(k), & for\ [N/2] < m < N \\ \sum_{k=1}^{N-1} H_{m,asy}(k), & for\ m = N \end{cases} \tag{4.22}$$

Sum of pair and asymmetric H-fields gives an approximated total H-field applied to the target wire. By using the obtained H-field values for each turn, proximity part of the overall resistor can be calculated as in (4.8).

In this proximity effect approach, H-field on a target wire is calculated at 3 different points, α, β and θ and in z-axis, so an approximation is applied. If the H-field is calculated at the other remaining points at y-axis in addition to z-axis, a much accurate proximity effect calculation is possible.

4.2 Inductance Calculation

Another critical design step is the calculation of self and mutual inductances of the transmitter and receiver coils. In the following subsections, self-inductance of the coils and their mutual inductance with respect to their relative positions, i.e. distance between coils and lateral misalignment of transmitter and receiver coils etc. will be analytically calculated. After that, analytical results will be compared with finite element analysis (FEA) results.

4.2.1 Self-Inductance Calculation

One example of a planar spiral coil configuration is shown in Figure 4.5. In this figure, N is the number of turns of the coil, p is the coil pitch that is the distance

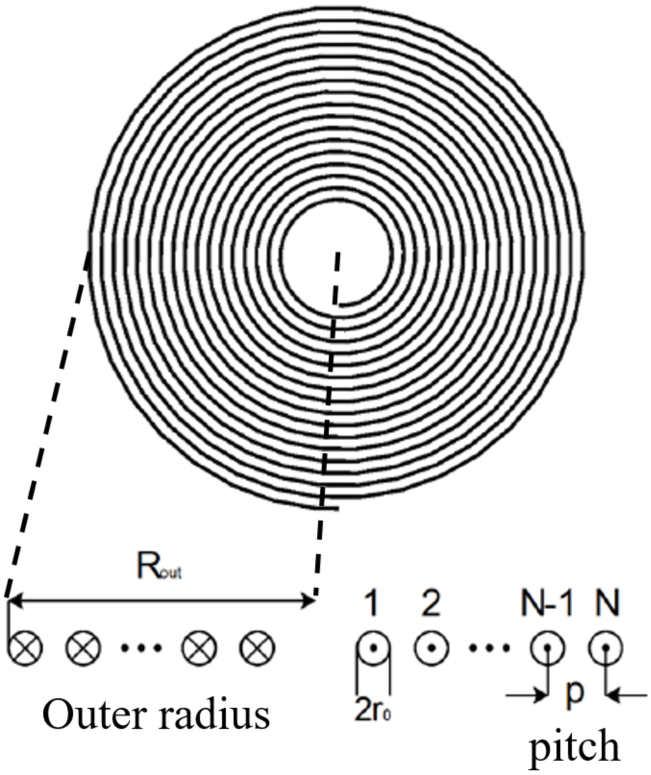

Figure 4.5: Planar spiral coil

between centers of two adjacent turns, R_{out} is outer radius of the coil and r_0 is the radius of the wire.

In order to calculate self inductance of a planar spiral coil, the following expression that is proposed in [23] is used in this study.

$$L = \begin{cases} \dfrac{N^2(2R_{out} - Np)^2}{32R_{out} + 28Np}\dfrac{39.37}{10^6}, & N >> 1 \\ \mu_0 R_{out}(ln\dfrac{8R_{out}}{r_0} - 2), & N = 1 \end{cases} \tag{4.23}$$

where μ_0 is the permeability in vacuum.

4.2.2 Mutual Inductance Calculation

Calculation of the mutual inductance is not as trivial as calculation of the self inductance of planar spiral coils because mutual inductance depends on the parameters that are related to relative positions of the coils such as lateral misalignment, angular misalignment, distance between coils etc. A model of two single turn circular coils is shown in Figure 4.6. Based on the derivations in [12], mutual inductance of those coils can be calculated as follows.

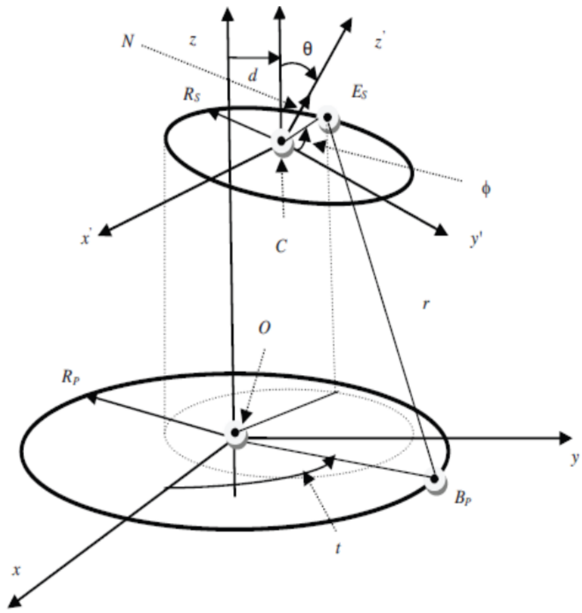

Figure 4.6: Two single turn coils with angular and lateral misalignment [12]

$$M = \frac{2\mu_0}{\pi}\sqrt{R_p R_s}\int_0^{\pi}\frac{(cos\theta - \frac{d}{R_s}cos\phi)\Psi(k)}{k\sqrt{V^3}}d\phi \tag{4.24}$$

$$\Psi(k) = (1 - \frac{k^2}{2})K(k) - E(k) \tag{4.25}$$

$$K(k) = \int_0^{\pi/2}\frac{1}{\sqrt{1 - k^2 sin^2\theta}}d\theta \tag{4.26}$$

$$E(k) = \int_0^{\pi/2}\sqrt{1 - k^2 sin^2\theta}d\theta \tag{4.27}$$

$$k^2 = \frac{4\alpha V}{(1 + \alpha V)^2 + \xi} \tag{4.28}$$

$$\xi = \beta - \alpha cos\phi sin\theta \tag{4.29}$$

$$\alpha = \frac{R_s}{R_p} \tag{4.30}$$

$$\beta = \frac{c}{R_p} \tag{4.31}$$

$$V = \sqrt{1 - sin^2\theta cos^2\phi + \frac{d^2}{{R_s}^2} - 2\frac{d}{R_s}cos\theta cos\phi} \tag{4.32}$$

where

μ_0: permeability of vacuum

R_p: radius of primary coil

R_s: radius of secondary coil

θ: angular misalignment

d: lateral misalignment

ϕ: angle of integration at any point of the secondary coil

α: shape factor of the coil's physical geometry

c: separation distance between coils

k: variable

$K(k)$: complete elliptic integral of the first kind

$E(k)$: complete elliptic integral of the second kind

Equation (4.24) can be used to calculate mutual inductance of two single-turn coils. In order to find the complete mutual inductance of the transmitter coil with N_{tx} and the receiver coil with N_{rx}, mutual inductance for each turn pair is calculated and summed to get the total mutual inductance as in (4.33).

$$M = \sum_{i=1}^{N_{tx}} \sum_{j=1}^{N_{rx}} M_{ij} \tag{4.33}$$

4.2.3 Validation of Analytical Results with FEA Results

Analytical expressions for resistances and inductances of coils are given in the previous subsections. In this section, analytical results for inductances will be compared

Table 4.1: Configuration parameters of FEA model of coils

	Transmitter	Receiver
Number of turns	5	6
Pitch (mm)	2.5	2
Radius of wire (mm)	0.5	0.35
Inner radius (mm)	25	25
Distance between coils (mm)	20	

with the FEA results. In order to do this, an FEA model that consist of transmitter and receiver coils is in ANSYS Maxwell. Generated FEA model is shown in Figure 4.7. Yellow coil is the transmitter coil and the green one is the receiver coil. Corresponding configuration data of the coils are listed in Table 4.1.

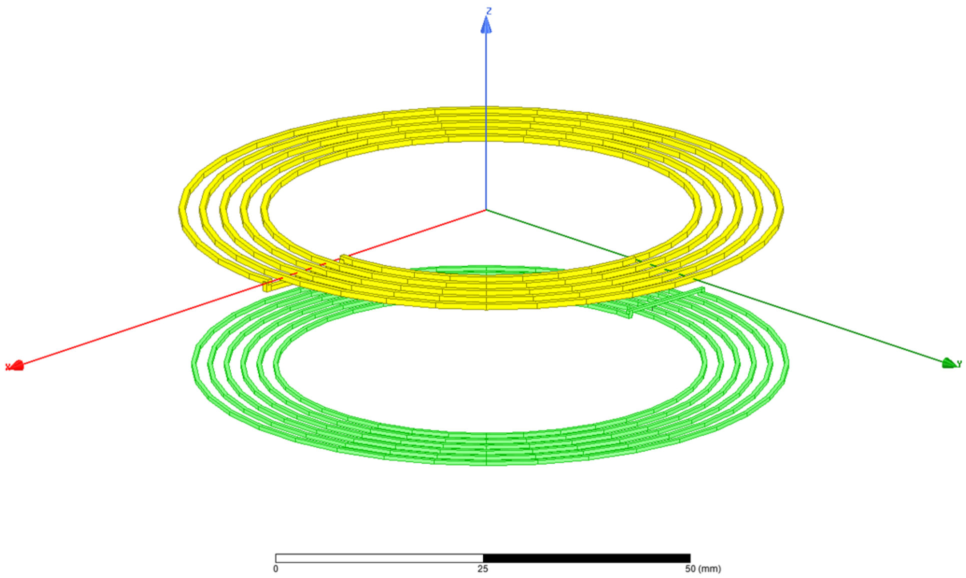

Figure 4.7: FEA model of transmitter and receiver coils

In order to validate the results, transmitter coil number of turns are swept from 5 to 15 turns while the other parameters are kept constant. Self inductance result comparison of FEA model and analytical calculation results is shown in Figure 4.8. The same validation method is used for mutual inductance calculation. Corresponding comparison result is shown in Figure 4.9.

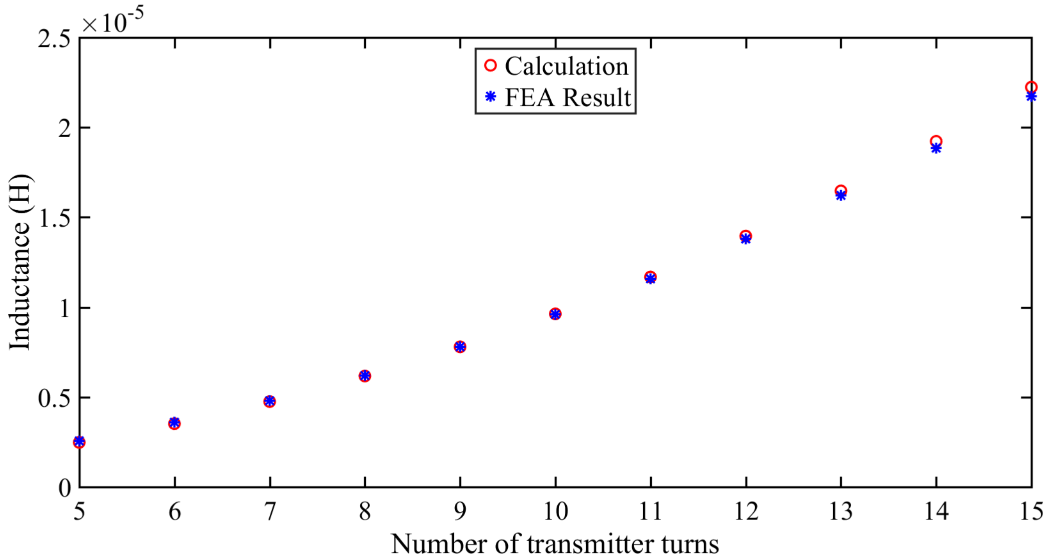

Figure 4.8: Analytical analysis and FEA results of self inductance with varying number of transmitter turns at transmitter inner radius of 25 mm

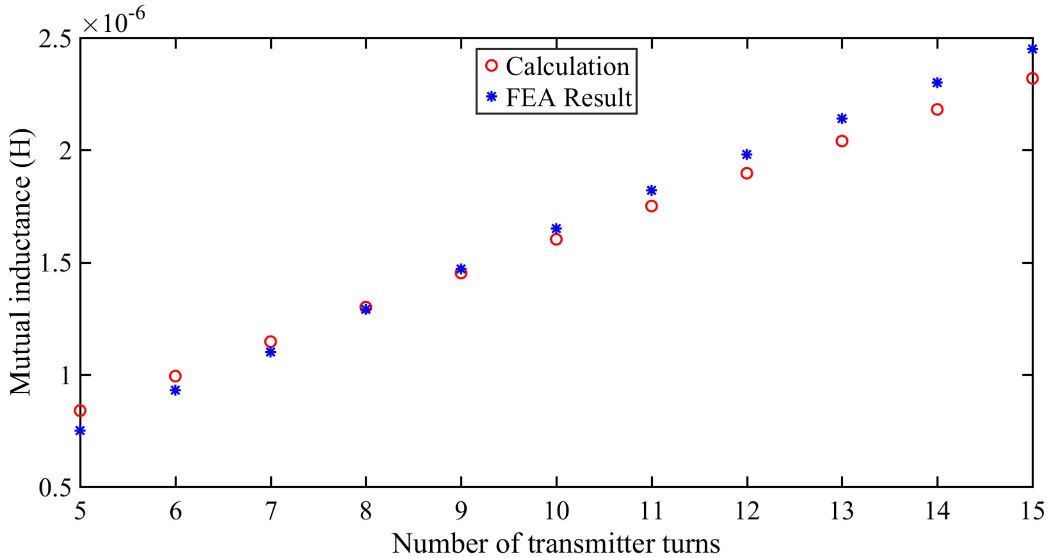

Figure 4.9: Analytical analysis and FEA results of mutual inductance

In addition to the calculation verification with number of turns sweep, self inductance calculation verification with varying inner coil radius values would be needed. That verification is shown in Figure 4.10. In this figure, again transmitter coil given in Table 4.1 is used and its inner radius is swept from 15 mm to 40 mm.

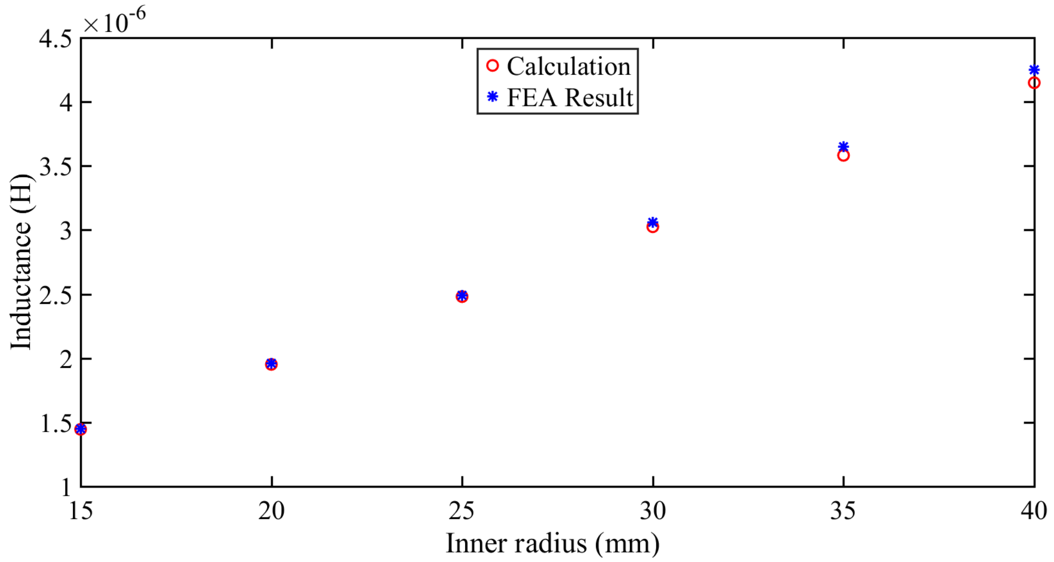

Figure 4.10: Analytical analysis and FEA results of self inductance with varying inner radius of the coil

In Figure 4.8, effect on number of turns on self inductance as in (4.23) is studied. Self inductance increase is expected with increasing number of turns and the analytical analysis and FEA results for variation of self inductance with respect to number of turns have a good match as seen in Figure 4.8. Results of another self inductance parameter, inner coil radius, are shown in Figure 4.10. Again, analytical analysis and FEA results coincide with each other with varying inner coil radius.

Mutual inductance value validation is made only for varying number of turns of transmitter. As seen in Figure 4.9, analytical analysis results and FEA results are pretty close to each other at 2 cm distance as listed in Table 4.1. Other effective parameters on mutual inductance, angular misalignment and lateral misalignment, are not considered in this thesis.

Resistance validation is not studied either because while calculating resistance of a Litz wire, strand to strand effects must be taken into account as explained in previous sections. However, ANSYS Maxwell ignores that effect for stranded wire resistance calculations. Therefore, analytical analysis for resistance will be compared with measurements in latter chapters.

CHAPTER 5

DESIGN, FEA ANALYSIS AND SIMULATION OF A 50W WIRELESS POWER TRANSFER SYSTEM

In this chapter, studied theory in previous chapters will be used to design a 50 W wireless charger system. First, system specifications for the wireless charger for charging the battery in a vest will be discussed. In the next steps, first, design methodology will be presented, and then 2 designs will be selected. Before test bench implementation of selected designs, characteristics of them will be simulated by using electrical simulation tool PLECS/PLEXIM.

5.1 System Specifications

The purpose of this thesis is to study and design a battery charger for a charging vest. Due to limited space available, maximum radius of the transmitter is selected to be as 100 mm and that of receiver is selected to be as 50 mm.

For the supply, 25 V input voltage is selected that can be easily obtained from a lead-acid battery in the vehicle. For the load, volume and voltage level of the battery pack are the design criteria. Volume of it is critical because it will be installed in a vest and the voltage level must be harmless to human body. Therefore, 12 V Li-ion batteries are chosen. Also, the distance between the transmitter and receiver coils is limited to maximum 5 cm and in the design process 2 cm distance is assumed.

Another design criterion is the operating (resonant) frequency of the system. In this study, maximum operating point is limited to 750 kHz. Higher frequencies in MHz region are avoided not to complicate PCB design.

Beside of all these criteria, power level of the system is another essential design specification for a WPT system because supply and load currents, coil currents, operating frequency etc. depend on output power. In this thesis, power level is chosen as 50 W. With this information, DC input and output currents can be calculated as $\sim$2 A and $\sim$4 A, respectively.

5.2 Design Methodology

Before explaining the design methodology, it's important to mention how planar spiral coils are implemented. In order to wind Litz wire as a proper spiral coil, coil frames were printed out from a 3-D printer. Receiver coil frame is shown in Figure 5.1. While designing frames, pitch is selected as 2.5 mm for transmitter coil and 2 mm for receiver coil.

Figure 5.1: Receiver coil frame

In order to analyze and compare possible designs with those frames, all the possible turn combinations are obtained for the transmitter and receiver coils. Self inductances and resistances of transmitter and receiver coils and mutual inductances of each pair of coils are calculated in Matlab. After having this data, next step is to find operating frequency for each coil pair. Resonance frequencies for each coil pair is found for 60 W output power. The reason why resonance frequencies are selected for 60 W will be explained in the latter sections.

As expected, there were too many designs to analyze and compare by hand. First, all the designs that have higher resonant frequency than 750 kHz are eliminated. Then, a Pareto-front search method is applied. Comparison criteria for Pareto-front search are selected as the efficiency degradation percentage with respect to distance variation and the efficiency degradation precentage with respect to resonance frequency mismatch. Efficiency degradations are obtained at 2 cm for nominal distance and at 3 cm for distance variation cases. For the resonance frequency mismatch, percentage efficiency change at resonance frequency and 90% of it are calculated. Corresponding Pareto-front search output is shown in Figure 5.2. Since both of the criteria are related to the efficiency degradation, it can be said that dots that are near to the origin are much better designs than the remainings in terms of efficiency degradation over misalignment and resonant frequency mismatch. In addition, there are two different colored dots in Figure 5.2, red dots show the designs with resonance frequencies higher than 750 kHz, which are eliminated. Black dots are the remaining designs, which can be selected.

In addition to the search given in Figure 5.2, extra searches were needed because the first search gives only the information on the efficiency degradation percentage but there is no efficiency information in this search. Therefore, efficiency filtering was applied to designs that are in the 0-4% range in both criteria. First filter was at 94%. Result of the filtering at 94% efficiency is shown in Figure 5.3. Almost all the results are red meaning they have resonance frequencies above 750 kHz. The remaining 4 designs are almost the same and difference in their resonance frequencies is very small to compare them in terms of shielding requirement. At this point, a conclusion can be made that as the frequency gets higher, efficiency of the system increases.

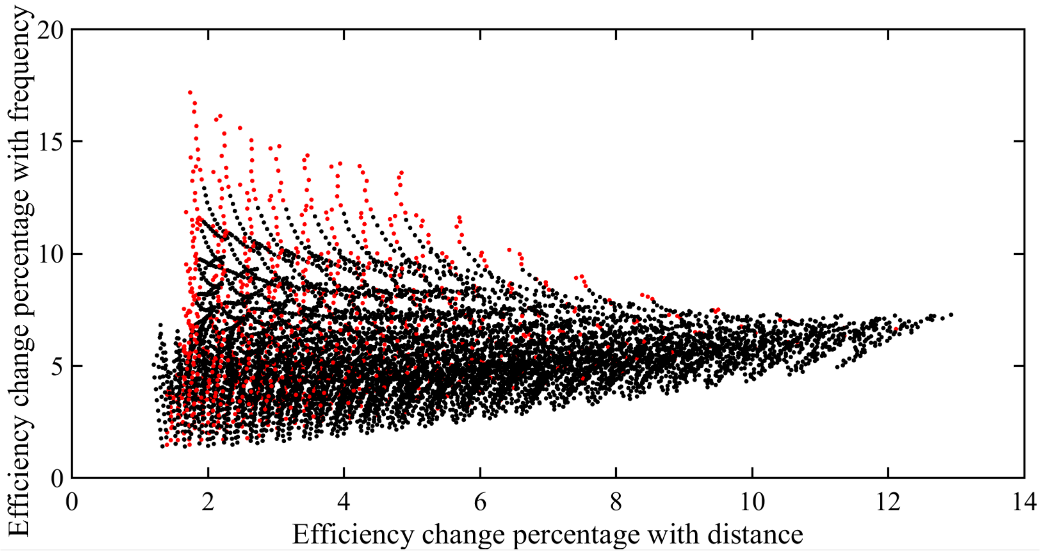

Figure 5.2: Pareto front search with regards to efficiency degradation with varying resonance frequency and with varying distance, red designs have higher resonance frequency than 750 kHz and black ones have lower resonance frequency than 750 kHz

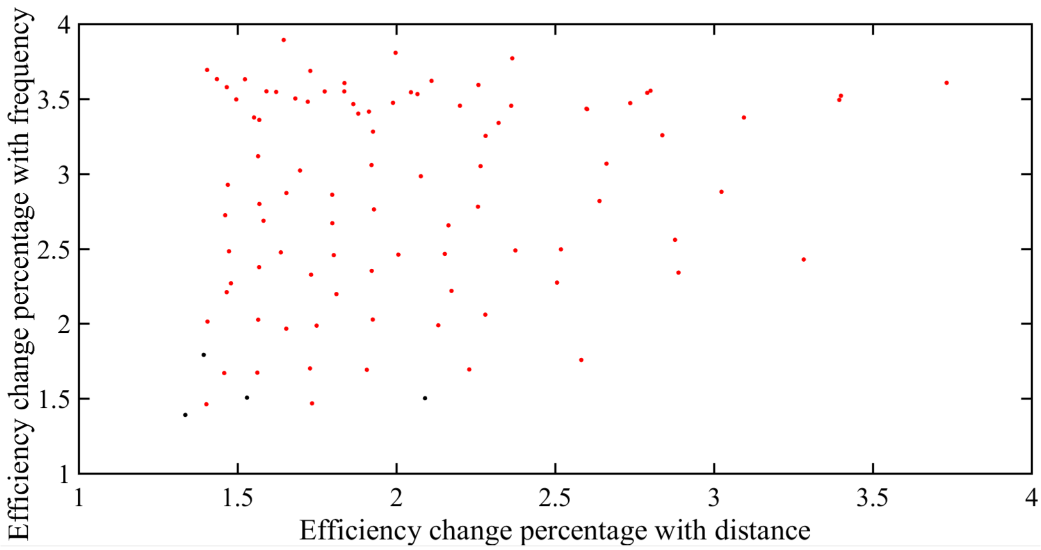

Figure 5.3: Filtering with 94% efficiency criterion, red designs have higher resonance frequency than 750 kHz and black ones have lower resonance frequency than 750 kHz

Since a selection could not be made after 94% efficiency filtering, efficiency filtering limit was reduced to 92%. Output of filtering at 92% efficiency is shown in Figure 5.4. The blue stars in this figure are the selected designs. One of them has resonance frequency at 500 kHz and the other one at 400 kHz, so difference in resonant frequencies is enough to compare the effect of frequency on shielding. Parameters of selected designs are given in Table 5.1.

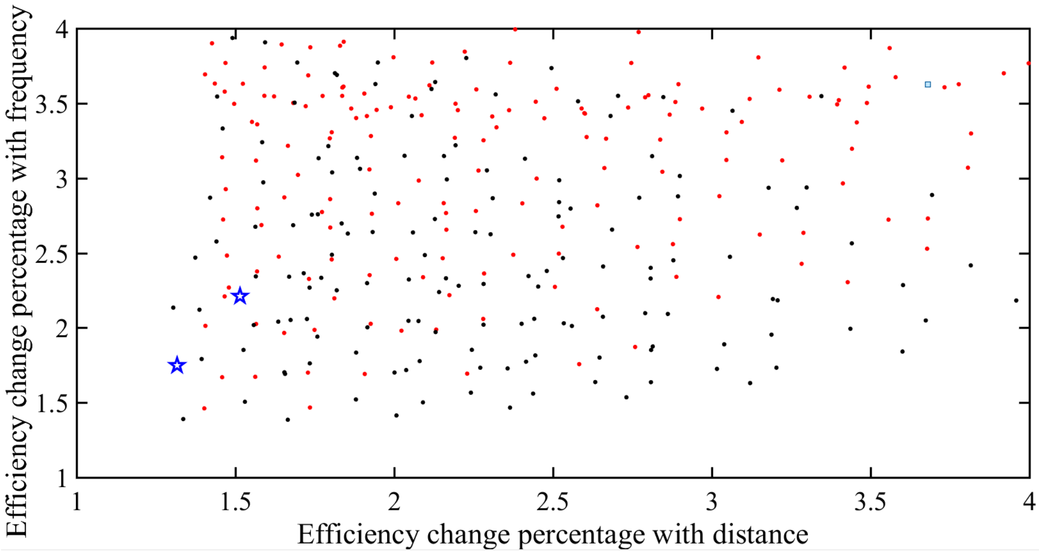

Figure 5.4: Filtering with 92% efficiency criterion, red designs have higher resonance frequency than 750 kHz and black ones have lower resonance frequency than 750 kHz, blue stars are selected designs

Table 5.1: Analytically calculated parameters of selected designs

	Coil pair 1		Coil pair 2	
	Transmitter	Receiver	Transmitter	Receiver
Inner radius (mm)	25	25	30	25
Number of turns	5	6	5	7
Self inductance (μH)	2.64	3.82	3.19	5.13
Mutual inductance @20 mm (μH)	0.776		0.984	
Mutual inductance @30 mm (μH)	0.576		0.735	
Resistance (mΩ)	44	74	50	78
Resonance frequency (kHz)	500		400	
Resonance capacitor (nF)	38.4	26.5	49.6	30.9
Output power (W)	60		60	

At this point, designs that will be implemented and tested, are determined. Now, it is better to check the output power behaviour with respect to their operating frequencies. As seen in Figures 5.5 and 5.6, 60 W output power is expected at resonance frequencies, at 500 kHz and 400 kHz, respectively. However, it is seen that both systems operate in bifurcation operation, which is mentioned in subsection 3.4. Figures 5.5 and 5.6 imply that target output power or more can be transmitted even if there is a resonant frequency mismatch or a misalignment but it will decrease the overall efficiency. Transferring required output power is more important than efficiency in our design, so these selected designs are fine. As mentioned earlier, bifurcation operation may require an extra effort while designing the controller. Controller solution for this system will be studied in a latter section.

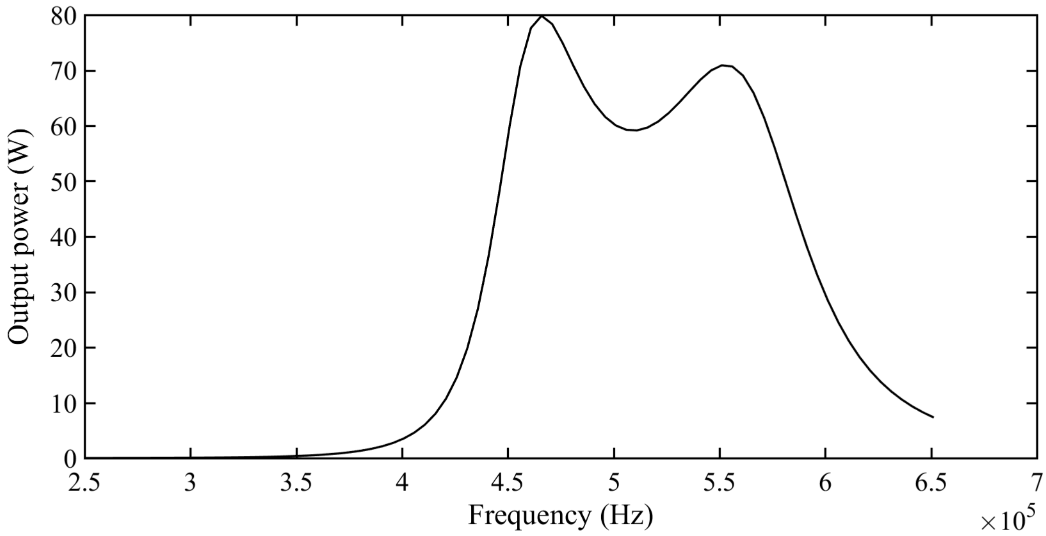

Figure 5.5: Output power variation of the design with 500 kHz with respect to operating frequency

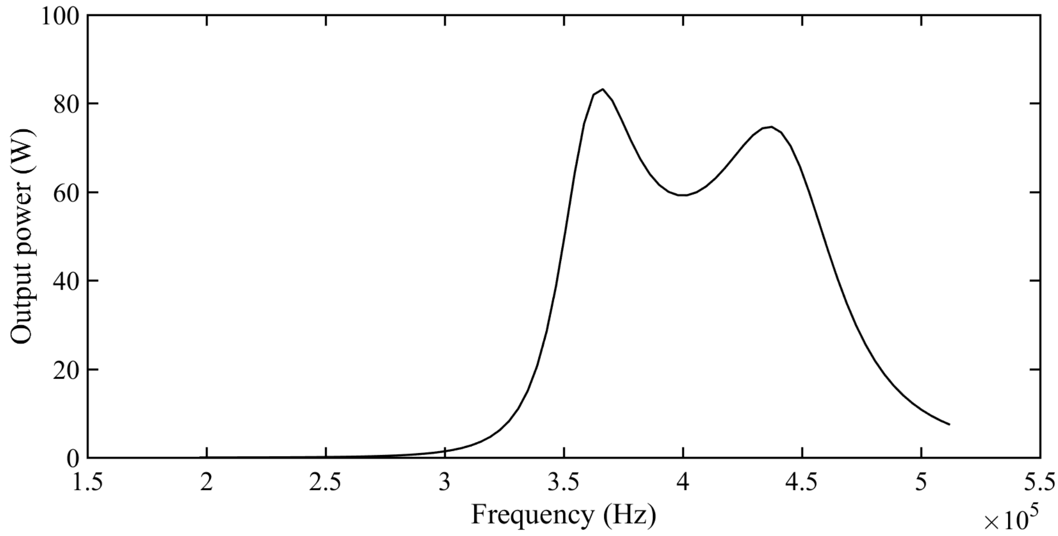

Figure 5.6: Output power variation of the design with 400 kHz with respect to operating frequency

5.3 Implementation of Coils

Self and mutual inductance analytical calculations have similar results with the FEA results. However, resistance calculation is not as easy as inductance calculation because the explained Litz wire resistance calculation method is for an ideal Litz wire. Thus, before a complete simulation for both systems, resistance values must be measured. In order to do that, both coils were implemented on the frames printed out by a 3D printer according to the selected designs of Pareto-front search output. For the transmitter coil, a Litz wire with 0.5 mm equivalent radius was used. Strand number of transmitter Litz is 100 and each strand has 0.1 mm diameter. For the receiver, a Litz wire with 0.35 mm equivalent radius is used. Strand number of receiver Litz wire is 50 and each strand has 0.1 mm diameter. Implemented coils can be seen in Figure 5.7. Pair with the white frames is implemented for the design with 500 kHz resonance frequency and the other one is implemented for the design with 400 kHz resonance frequency.

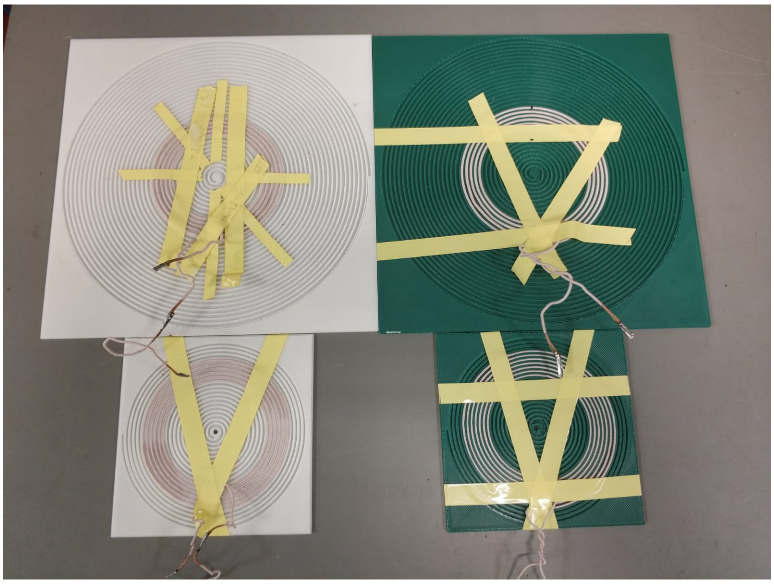

Figure 5.7: Implemented coils

To measure the self and mutual inductances, HIOKI IM 3533 LCR METER is used. Measurement frequency of HIOKI is limited to 200 kHz but inductance values don't have a strong dependency of frequency. Therefore, self and mutual inductances were measured at 200 kHz and assumed as constant at 400 and 500 kHz frequencies. On the contrary to inductance, resistance value changes dramatically with frequency. Therefore, their resistance measurement were done by Agilent E4980A at corresponding resonance frequencies. Sample pictures for both measurements are shown in Figure 5.8 and Figure 5.9 and obtained measurement results for both coil pairs are tabulated in Table 5.2. The reason why the resistance results in Figure 5.8 and Table 5.2 are different is the fact that their measurement frequencies are different than each other.

Table 5.2: Resistor and inductor measurement results

	Coil pair 1 @ 500 kHz		Coil pair 2 @ 400 kHz	
	Transmitter	Receiver	Transmitter	Receiver
Resistance $(m\Omega)$	108.07	154.24	123.85	201.78
Inductance (μH)	2.55	3.85	3.20	4.95
Mutual inductance @20mm (μH)	0.72		0.99	
Mutual inductance @30mm (μH)	0.55		0.63	

Figure 5.8: Inductance and resistance measurement of transmitter coil of design with 400 kHz resonance frequency at 200 kHz

As can be concluded by comparing Table 5.1 and Table 5.2, there is a big mismatch between AC resistance measurement and calculations. The reason why the measurement and analytical calculation results are very different is that the used Litz wire is not an ideal Litz wire. Thus, internal induced resistance is much bigger than the calculations, so the overall resistance.

On the contrary to resistance calculation, inductance measurement results are very similar to the analytical inductance calculation as can be seen in Tables 5.1 and 5.2. The main reason of it is that inductance varies with frequency slightly, so this variation is neglected during design and verification.

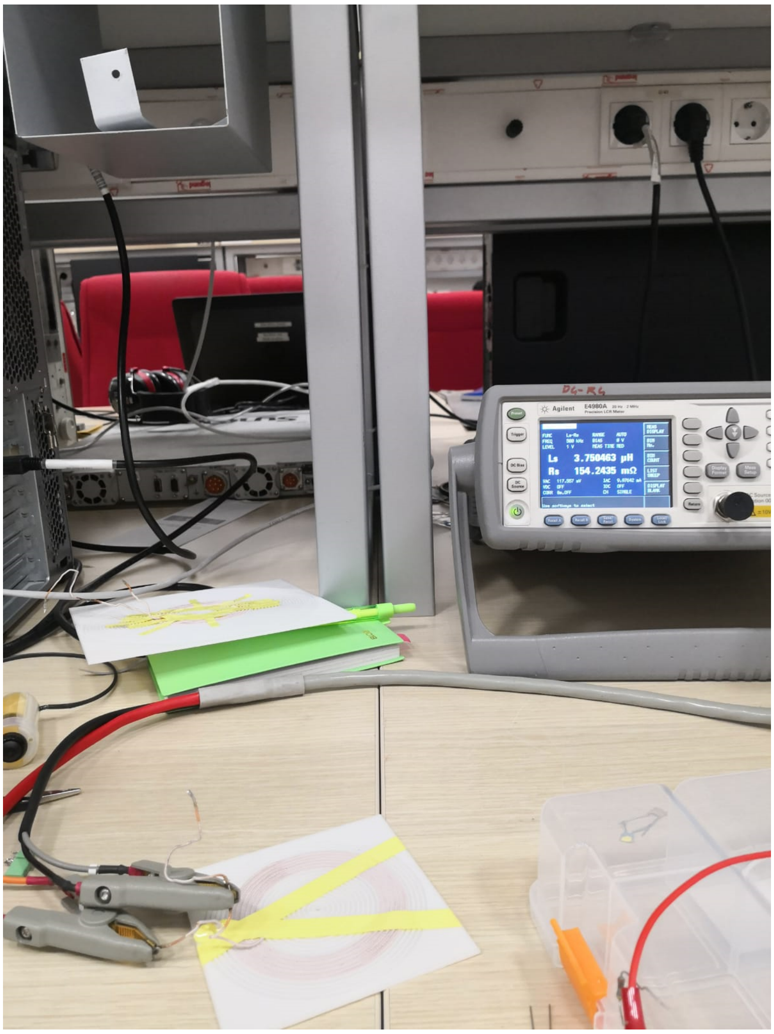

Figure 5.9: Inductance and resistance measurement of the receiver coil of the design with 500 kHz resonance frequency

5.4 Simulation Results of Selected Designs

In order to get a more practical result, the selected systems are simulated by using PLECS simulation tool. In the simulation models, theoretically calculated self and mutual inductances are used because there is not much difference between calculated and measured values. However, difference between calculated and measured resistance values cannot be underestimated. Therefore, measured resistance values are used in the simulations.

Simulations are conducted with 3 different loads. First, pure resistive load is used and this will be a typical WPT system simulation. However, pure resistive load is not a realistic simulation for a battery charger. This is because of that sinusoidal current passes through the resistive load, so a rectifier is needed. Moreover, a battery cannot be effectively charged with a high frequency rectified sine wave current. Therefore, in order to filter high frequency component of the receiver current, a resistive load with an LC filter is simulated. Finally, a battery charging case with a controller is simulated.

5.4.1 Resistive Load

Design with 500 kHz resonance frequency:

Simulation schematic structure for the design with 500 kHz resonance frequency with resistive load is shown in Figure 5.10. Self and mutual inductance syntax is in the form of [L1, M; M, L2] in the figure. For the sake of simplicity, a square wave generator is used instead of a half bridge switching circuit. Corresponding simulation results are shown in Figure 5.11 and numerical data is given in Table 5.3.

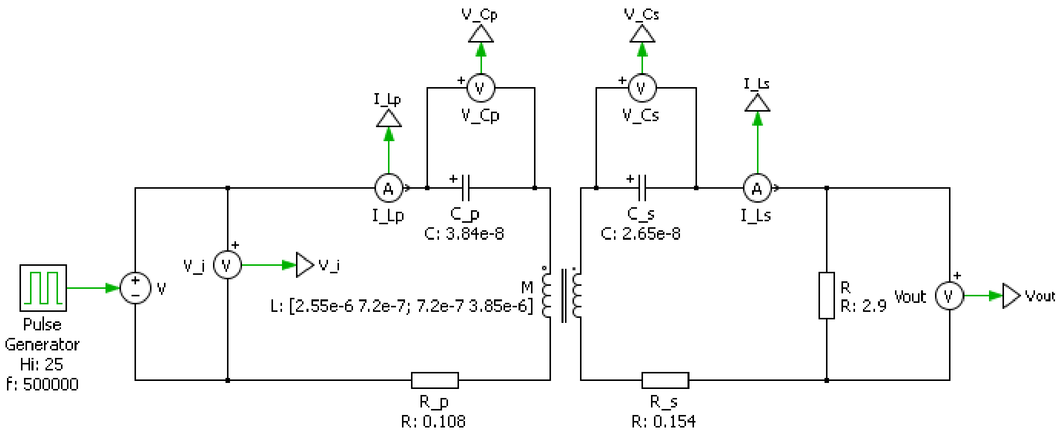

Figure 5.10: Simulation schematic of the design with 500 kHz resonance frequency with resistive load

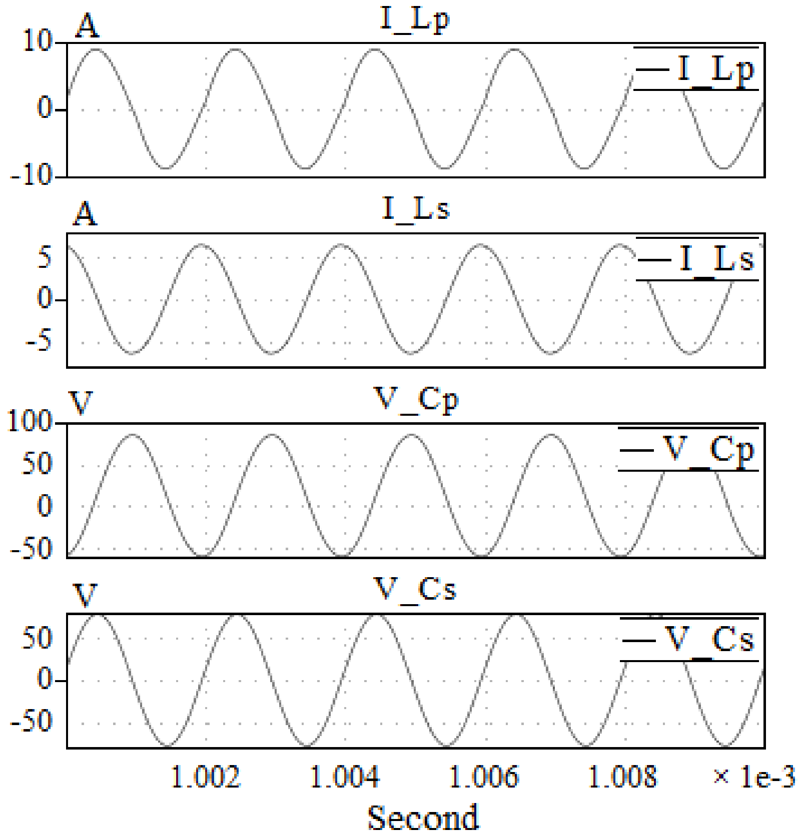

Figure 5.11: Primary coil current, secondary coil current, primary capacitor voltage, secondary capacitor voltage for the design with 500 kHz frequency

Table 5.3: Simulation results for the design with 500 kHz resonance frequency with resistive load

	Simulation results
Primary coil current (A_{rms})	6.21
Secondary coil current (A_{rms})	4.6
Output power (W)	61.38
Efficiency ($\%$)	89.23

Design with 400 kHz resonance frequency:

Simulation schematic structure for the design with 400 kHz resonance frequency with resistive load is shown in Figure 5.12.

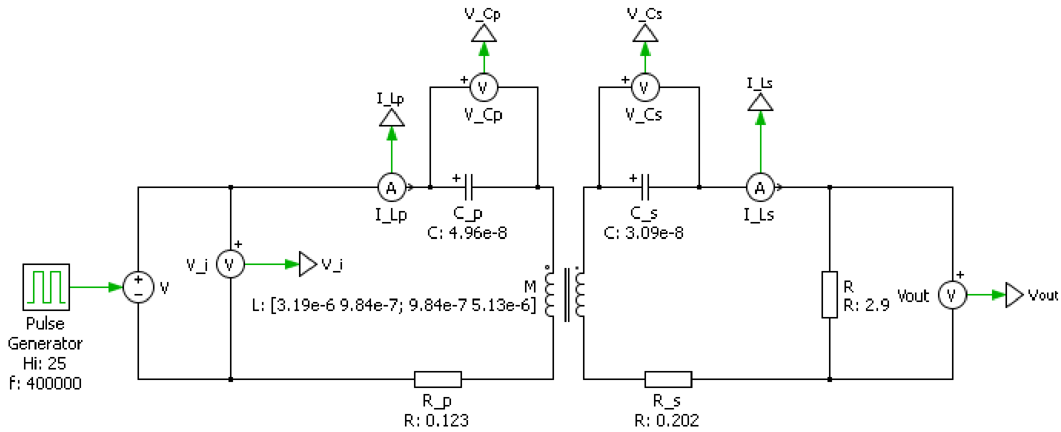

Figure 5.12: Simulation schematic of the design with 400 kHz resonance frequency with resistive load

Corresponding simulation results are shown in Figure 5.13 and numerical data is given in Table 5.4.

Table 5.4: Simulation results for design with 400 kHz resonance frequency with resistive load

	Simulation results
Primary coil current (A_{rms})	5.38
Secondary coil current (A_{rms})	4.28
Output power (W)	53.21
Efficiency $(\%)$	88

After the Pareto-front search, efficiencies of selected designs are estimated to be higher than 92%. However, in Tables 5.3 and 5.4, efficiency values for both designs are lower than expected. This is because of that analytical calculation results of coil resistance, which are used while designing, is much lower than the measured resistance values, which are used as simulation parameters. Miscalculation of the coil resistances caused to have a lower-efficiency design than expected.

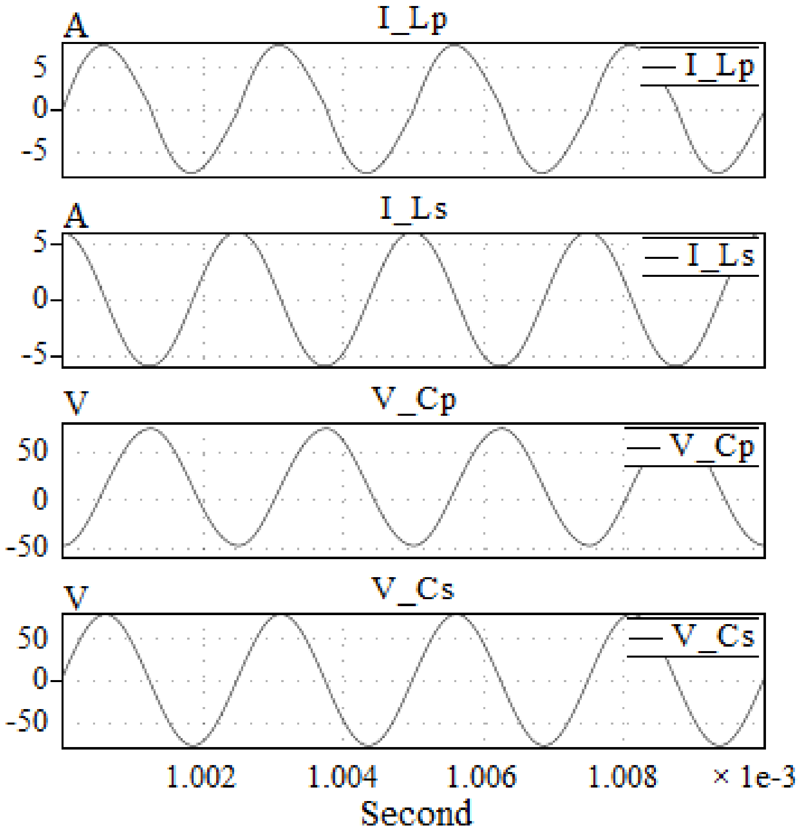

Figure 5.13: Primary coil current, secondary coil current, primary capacitor voltage, secondary capacitor voltage for the design with 400 kHz frequency

5.4.2 Resistive Load with LC Low-Pass Filter

In this part, a full wave rectifier diode is added to the load side in order to rectify sinusoidal secondary coil current. In addition, an LC low-pass filter is added at the end of the rectifier diodes in order to filter high frequency component of the load current.

<u>Design with 500 kHz resonance frequency:</u>

Simulation schematic structure for the design with 500 kHz resonance frequency with resistive load with a rectifier and LC filter is shown in Figure 5.14. Corresponding simulation results are shown in Figure 5.15. In Table 5.5, numerical results for both resistive load and filtered resistive load cases are compared. As seen in Table 5.5, LC filter does not have a big impact on secondary coil current and efficiency. However, since average secondary coil current passes through the load, output power is lowered and it's is nearly 50W, which is target output power. In addition, since output power is lowered and efficiency is remained nearly the same, transmitter coil current is lowered.

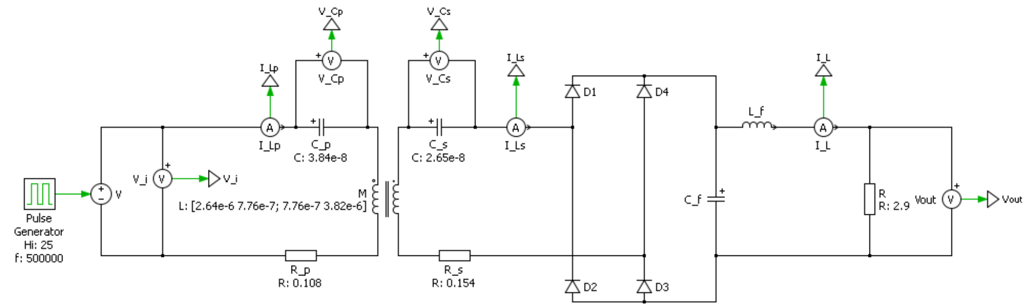

Figure 5.14: Simulation schematic of the design with 500 kHz resonance frequency with resistive load with LC filter

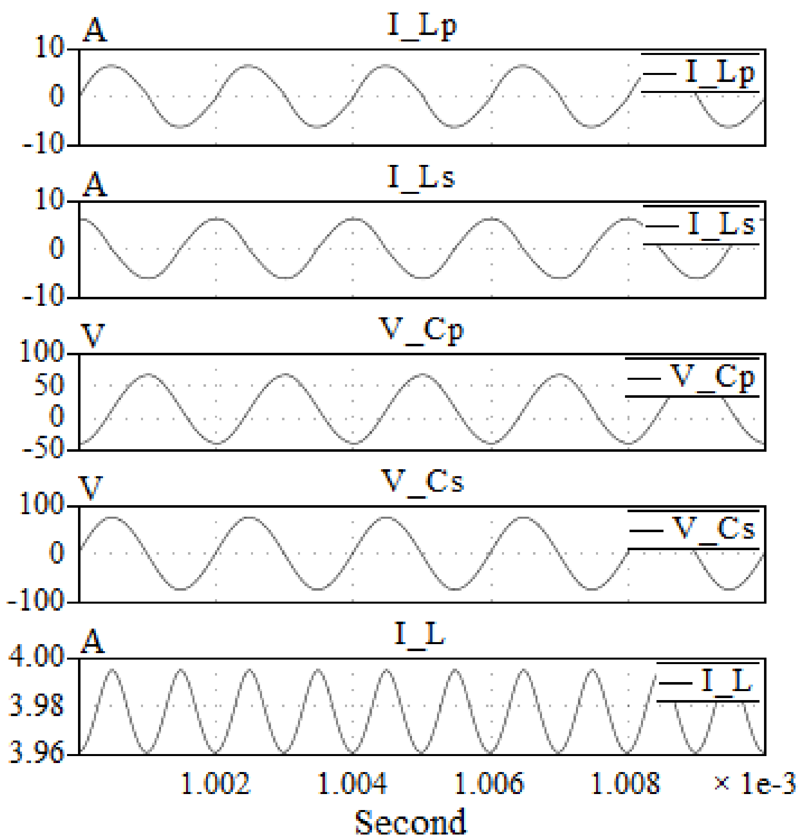

Figure 5.15: Primary coil current, secondary coil current, primary capacitor voltage, secondary capacitor voltage, load current for the design with 500 kHz resonance frequency with resistive load with LC filter

Table 5.5: Simulation results for the design with 500 kHz resonance frequency with resistive load and resistive load with LC filter

	Resistive load	Resistive load with filter
Primary coil current (A_{rms})	6.21	4.53
Secondary coil current (A_{rms})	4.6	4.42
Output current	4.6 A_{rms}	4 A_{avg}
Output cower (W)	61.38	45.86
Efficiency ($\%$)	89.23	89.8

Design with 400 kHz resonance frequency:

Simulation schematic structure for the design with 400 kHz resonance frequency with resistive load with rectifier and LC filter is shown in Figure 5.16 and simulation results are shown in Figure 5.17. In Table 5.6, again the numerical results for both resistive load and filtered resistive load cases are given.

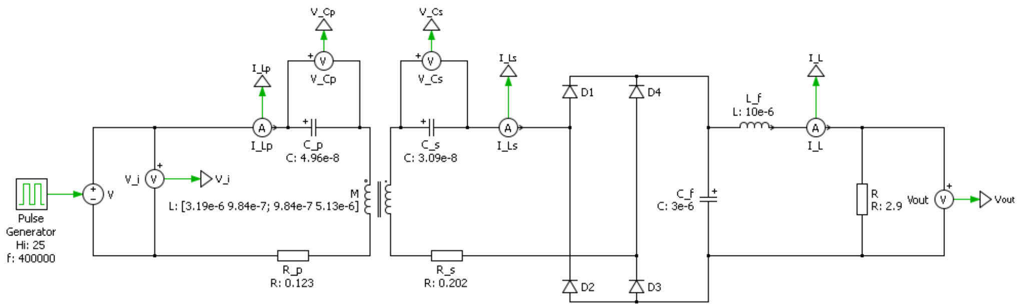

Figure 5.16: Simulation schematic of the design with 400 kHz resonance frequency with resistive load with LC filter

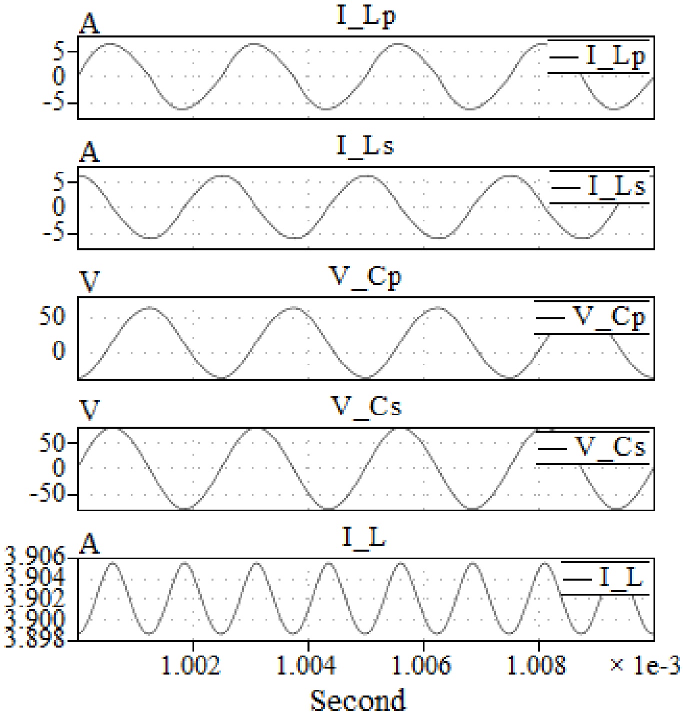

Figure 5.17: Primary coil current, secondary coil current, primary capacitor voltage, secondary capacitor voltage, load current for the design with 500 kHz resonance frequency with resistive load with LC filter

Table 5.6: Simulation results for the design with 400 kHz resonance frequency with resistive load and resistive load with LC filter

	Resistive load	Resistive load with filter
Primary coil current (A_{rms})	5.38	4.48
Secondary coil current (A_{rms})	4.28	4.33
Output current	4.28 A_{rms}	3.9 A_{avg}
Output power (W)	53.21	44.15
Efficiency ($\%$)	88	87.6

5.4.3 Battery Load

In this part, in addition to rectifier diodes and low-pass filter, a switching circuit is added to the receiver side.

Design with 500 kHz resonance frequency:

Simulation schematic structure for the design with 500 kHz resonance frequency with battery load is shown in Figure 5.18. Load current and output voltage variation over time for the same structure is shown in Figure 5.19. In order to simulate a battery, a 10 mF capacitor is placed to the load side with 50 mΩ series resistance. Also, initial voltage of the capacitor is defined as 9.5 V.

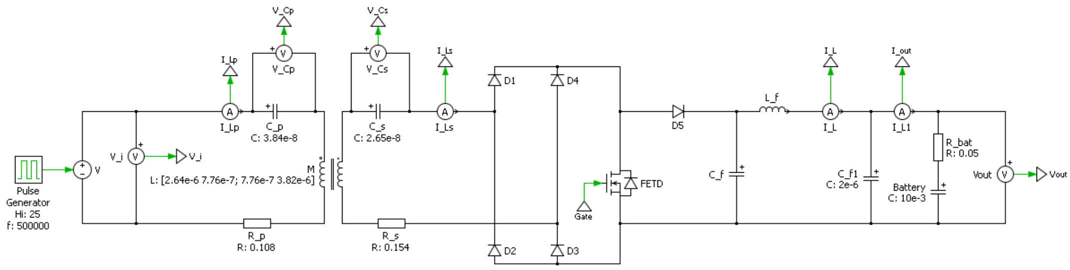

Figure 5.18: Design with 500 kHz resonance frequency with battery load

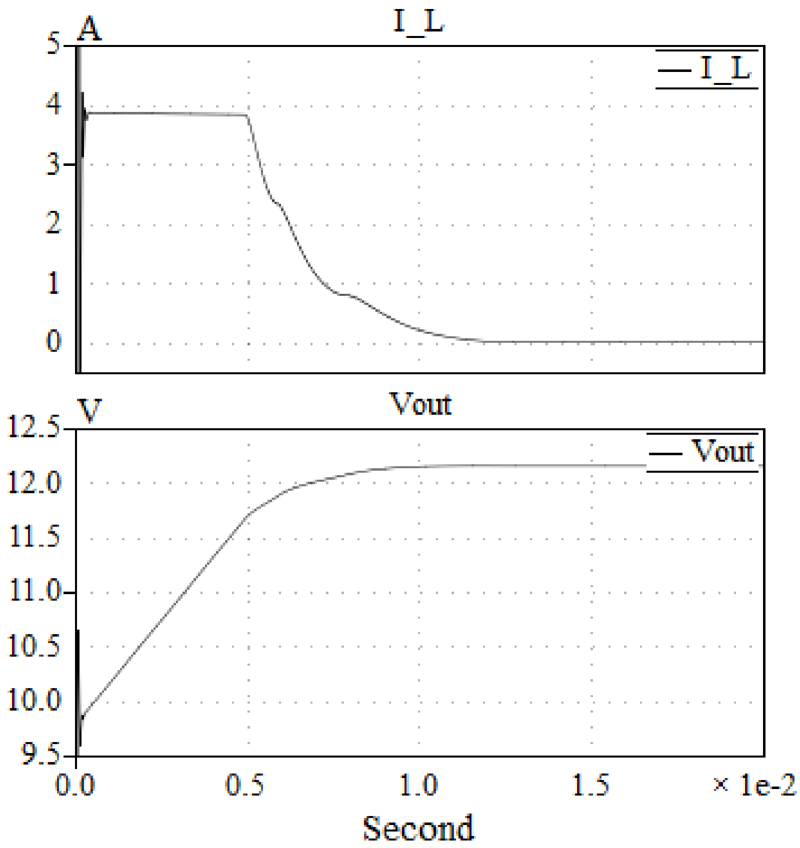

Figure 5.19: Load current and output voltage for the design with 500 kHz resonance frequency

Design with 400 kHz resonance frequency:

Simulation schematic structure for the design with 400 kHz resonance frequency with battery load and its results are shown in Figures 5.20 and 5.21, respectively.

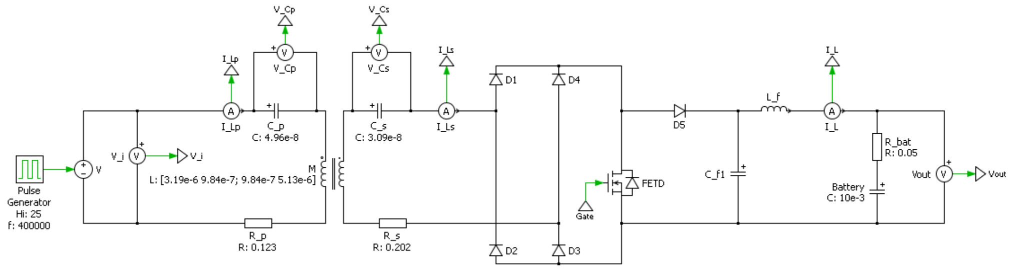

Figure 5.20: Load current and output voltage for the design with 400 kHz resonance frequency

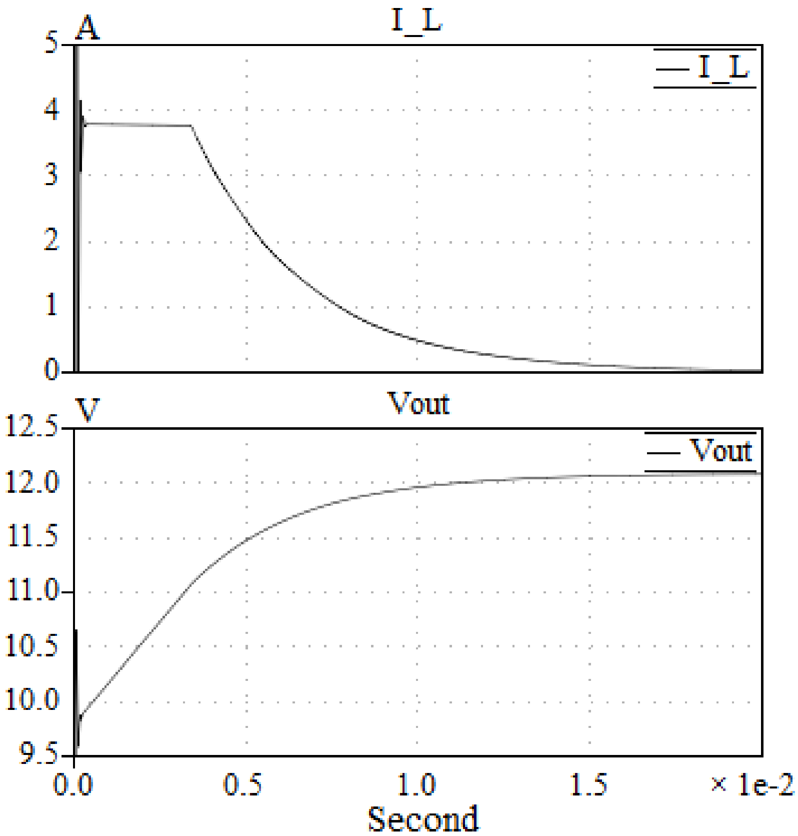

Figure 5.21: Load current and output voltage for the design with 400 kHz resonance frequency

Controller Structure

Controller structure for the battery management system can be seen in Figure 5.22. It consists of two parallel limiters, where one of them is for the output voltage and the other one is for the load current. Both controllers are basic PI controllers and they operate as an inverted form of a buck controller. Reference of the voltage loop is selected as 12 V and the reference of the current loop is selected as 4 A. When the battery voltage is much lower than the reference, 4 A limited current loop operates, which can be seen in the starting region in Figures 5.19 and 5.21 . After a while, as the output voltage gets closer to the voltage reference, voltage loop becomes active and lowers the output current. With this controller structure, increasing output current and output power in bifurcation operation became controllable and limitable. In addition to the current limit, maximum battery voltage is limited with a reference voltage. Another advantage of this controller is that there is no need for communication between transmitter and receiver for feedback.

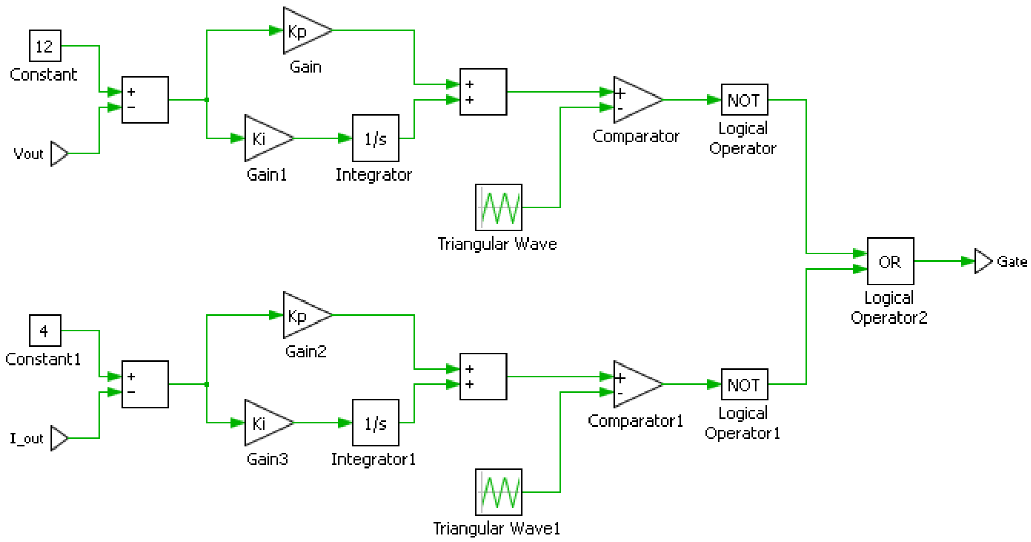

Figure 5.22: Controller of receiver switching circuit

Selected WPT systems are simulated at different cases. Simulation test case implementations and tests will be mentioned in the next chapter. In addition, similarities and differences between simulation results and test results will be studied.

CHAPTER 6

IMPLEMENTATION OF A 50 W WIRELESS BATTERY CHARGER

The selected designs are implemented and tested to validate analytical and numerical calculation results. Details on the design of transmitter and receiver coils are given in previous chapter. Design and implementation of compensation circuits and test results of the WPT systems are presented in this chapter.

6.1 Schematic and PCB of the WPT System

Basic structure of the implemented WPT system is shown in Figure 6.1. In order to drive transmitter resonant tank, half bridge switch configuration, $Q1$ and $Q2$, is used. As half bridge switches, a power MOSFET of Texas Instruments, CSD19531Q5A, is used. Before bypass capacitors, C_{bp}, of the half bridge, in order to filter input current, differential mode inductor, L_f, is used and as C_{in}, electrolytic and ceramic capacitor are used. At the receiver side, as rectifier diodes and switching circuit diode V12P10 schottky diode from Vishay is used. As MOSFET, the one used in the transmitter side MOSFET, CSD19531Q5A is used. In the following stage, a pi filter implemented in order to filter high frequency component of the battery current.

Design schematic and PCB is created on Altium Designer ECAD software. Printed board is shown in Figure 6.2. As seen in the figure, the board is split into transmitter and receiver sides. In the upper side of the transmitter side, input connectors and electrolytic capacitors are shown. In the other parts, filter inductor 7443550101 from Würth and half bridge switches can be seen. Half bridge switches are named as "HB". Finally, transmitter coil connectors and compensation capacitors can be seen.

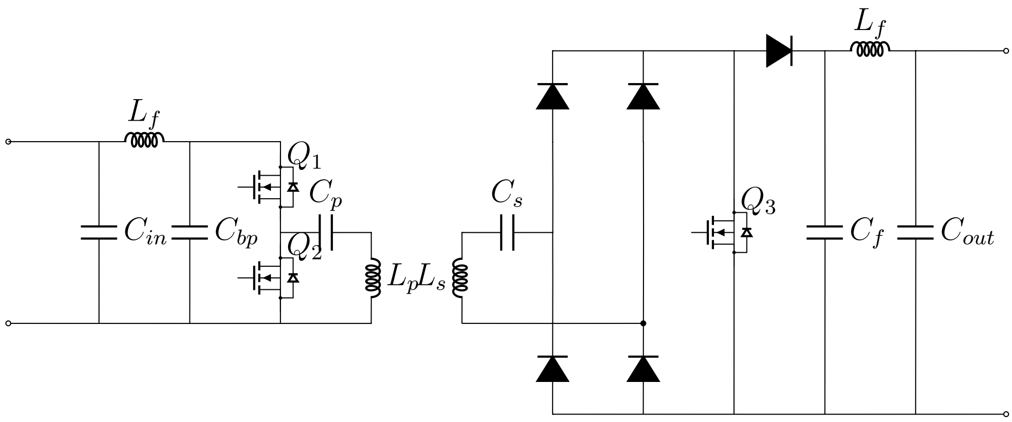

Figure 6.1: Basic schematics of the WPT system

In the middle of the board, the connector of the microcontroller is shown. As a microcontroller Piccolo TMS320F28035 Isolated controlCARD from Texas Instruments is used.

In the receiver part of the board, receiver coil connectors are shown in the upper part of the PCB. Resonant capacitors follow receiver coil connectors. Rectifier diodes, switching circuit and pi filter is laid between capacitors and output connectors.

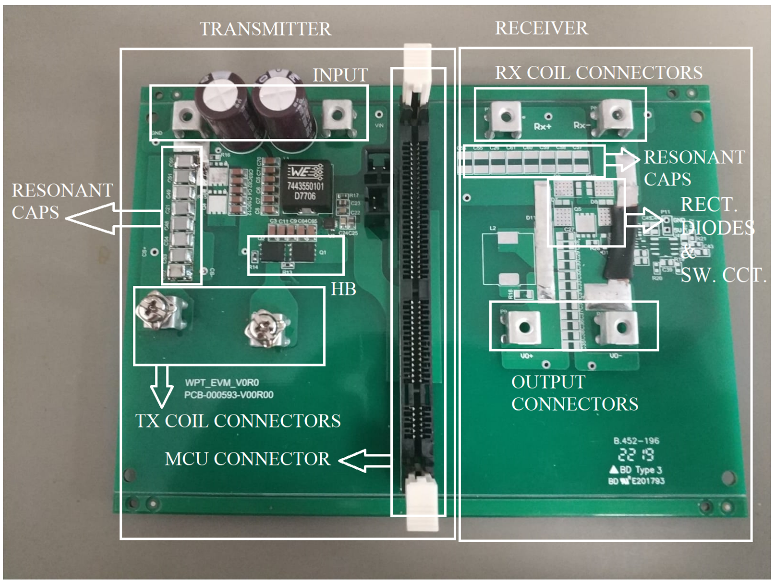

Figure 6.2: PCB

While designing the PCB, extra care was taken for gate-source and drain-source loops. Since the systems are driven at high frequencies, a bad layout may cause problems while driving it. In addition, operating at resonance is very important for WPT systems so any extra layout inductance would affect the resonance point. Therefore, this point was another critical point on layout. Another crutial point was to obtain symmetrical resonant capacitor placement. Since there are several parallel resonant capacitors, each of them should be equally affected by layout resistance and inductance.

6.2 Test Setup

Test setup is shown in Figure 6.3. On the upper left blocks, the power supplies for the input of the WPT system, fan, gate driving circuit and MCU are seen. For this purpose, three GWINSTEK GPD-33033 power supplies are used.

At the bottom of Figure 6.3, transmitter and receiver circuits and coils are shown. At the output of the receiver, batteries are placed. As the battery, 4 parallel BP7-12 model of B.B.Battery are used.

In order to measure coil current, a current probe which can measure high frequency current is needed, since the operating frequencies are 400 kHz and 500 kHz. For this purpose, 2 different Tektronix TCPA300 current probes are used for both transmitter and receiver coil currents.

For input and output DC voltage measurements, Fluke 115 multimeters are used. Multimeters are directly connected to the input and output pins in order to eliminate line voltage drops.

Finally, to observe all the voltages and currents, Tektronix TPS2024B oscilloscope is used. All the measurement devices and supplies are calibrated in laboratories that are accredited according to TS EN ISO/ IEC 17025:2012 standards.

6.3 Test Results and Validation

After the selected designs are implemented, they both tested at resistive load with and without pi-filter at 500 kHz and 400 kHz operating frequencies, as in the simulation

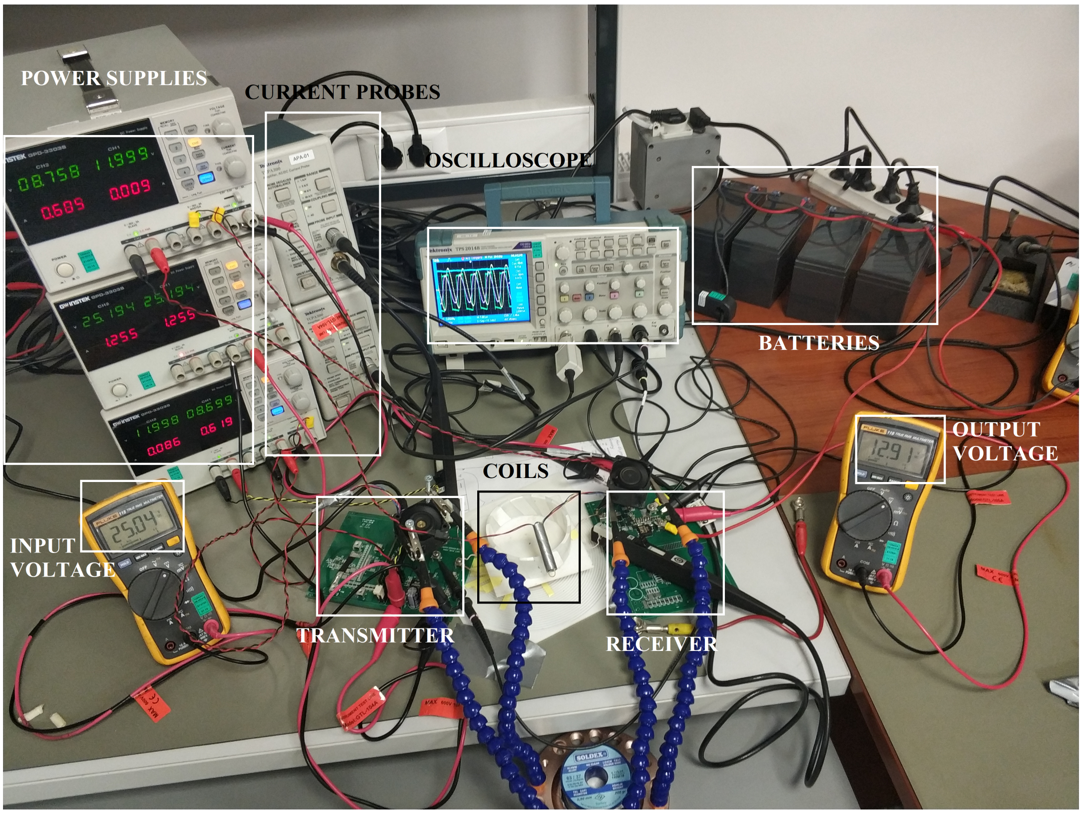

Figure 6.3: Test setup

case. For each design, conducted tests are listed as below:

Test 1: The system is tested at the nominal case with 2 cm distance between transmitter and receiver, no lateral misalignment and 25 V input voltage.

Test 2: The distance between transmitter and receiver is increased to 3 cm from 2 cm and there is again no lateral misalignment. However, since the systems operate in bifurcation and current limiting switching circuit was disabled, transferred power and the losses increase beyond the system limits when 25 V is applied from primary. Therefore, these tests were conducted at 19 V input voltage

Test 3: The distance between transmitter and receiver is kept its 2 cm and coils were placed at 25% lateral misalignment. Misalignment percentage is defined in a way that 50% misalignment is the point that center of the receiver is aligned with the last turn of the transmitter. This test was also conducted at 19V input voltage to avoid overheating.

Test 4: This is the nominal case with reduced voltage that is 2 cm distance and no lateral misalignment but at 19 V input voltage. This test is conducted to compare nominal case with misalignment case tests without any input voltage difference.

After resistive load tests, full wave rectifier diodes and pi-filter network are enabled and same tests were conducted again. For all tests, input voltage, input current, transmitter and receiver currents are measured. RMS value of the output voltage is measured by oscilloscope for resistive load and its average value is measured by using digital multimeter in filtered resistive load case. Obtained results for both designs are shown in Table 6.1 and Table 6.2

Table 6.1: Test results of the design with 500 kHz resonance frequency

	Resistive load				Resistive load with pi filter			
	Test 1	Test 2	Test 3	Test 4	Test 1	Test 2	Test 3	Test 4
Input voltage (V)	25	19	19	19	25	19	19	19
Input current (A)	2.96	5.29	4.17	2.31	2.3	4.34	3.38	1.76
Tx coil RMS current (A)	8.98	16.5	13	7	6.77	12.7	9.95	5.2
Rx coil RMS current (A)	4.03	4.43	4.02	3.1	4.04	4.61	4.15	3.02
RMS output voltage (V)	14.3	15.7	14.3	11	-	-	-	-
Mean output voltage (V)	-	-	-	-	11.65	13.3	11.94	8.73
Output current (A)	4.03	4.43	4.02	3.1	3.94	4.48	4.05	3.01
Output power (W)	57.63	69.5	57.5	34.1	45.9	59.6	48.4	26.3
Input power (W)	74	100.6	79.3	44	57.5	82.4	64.3	33.4
Efficiency (%)	78	69	72.5	77.5	79.8	72.4	75.2	78.8

For the comparison of simulation and test results for the design with 500 kHz resonance frequency, Tables 5.5 and 6.1 can be compared. In simulations, only Test 1 cases for both resistive load and filtered resistive load are simulated. As seen in these tables, first discussion point is the output power. For the nominal case, expected output power for both designs for resistive load was 60 W. However, obtained results are 57.63 W for design with 500 kHz resonance frequency and 50.76 W for design with 400 kHz resonance frequency. Degradation of the output power is caused by several factors. One of them is resistance values of the coils. Output power is lower than expected value, since coil resistance values are measured much higher than the analytical calculations. Another effective point is the losses of the semiconductors.

Table 6.2: Test results of the design with 400 kHz resonance frequency

	Resistive load				Resistive load with pi filter			
	Test 1	Test 2	Test 3	Test 4	Test 1	Test 2	Test 3	Test 4
Input voltage (V)	25	19	19	19	25	19	19	19
Input vurrent (A)	2.64	4.54	3.85	1.88	1.91	3.6	3.1	1.44
Tx voil RMS vurrent (A)	7.84	13.6	11.5	5.63	5.48	10.4	8.8	4.15
Rx voil RMS vurrent (A)	3.76	4.07	3.81	2.99	3.54	4.13	3.8	2.9
RMS output voltage (V)	13.5	14.6	13.6	9.8	-	-	-	-
Mean output voltage (V)	-	-	-	-	10.61	12.31	11.44	8
Output vurrent (A)	3.76	4.07	3.81	2.99	3.62	4.16	3.91	2.75
Output power (W)	50.8	59.4	51.8	29.3	38.4	51.2	44.7	21.9
Input power (W)	66	86.3	72.9	35.5	47.7	68.5	58.3	27.5
Efficiency ($\%$)	76.9	69	71	82.5	80.5	74.8	76.8	80

While designing the systems, semiconductor losses are assumed to be zero for the sake of simplicity. Numerical analysis of the losses will be studied in detailed in the next section.

Another comparison point is the efficiency. In simulation results, efficiency is found to be as 89% but in test results, it is found as 78%. The reason of it is that additional losses are neglected in simulations such as semiconductor losses. Consequently, transmitter current is measured much higher than the simulation results.

For the resistive load and filtered load comparison, the amounts of decrease of the output power are pretty close in simulation and test results. For both case, the output power with filtered resistive load case nearly equal to 75% of the output power with resistive load case. With this result, effect of filtering is validated by both simulations and tests.

Same conclusions that are made to compare Tables 5.5 and 6.1 can be done for the design with 400 kHz resonance frequency by using Tables 5.6 and 6.2.

Sample oscilloscope screens from measurements of 400 kHz and 500 kHz systems for filtered resistive load tests are shown in Figures 6.4 and 6.5, respectively. In these figures, yellow is the receiver coil current, blue is the output current, pink is the transmitter current and green is the half bridge switching node voltage. The most critical point in these figures is the phase difference between half bridge switching node voltage and transmitter current. In Figure 6.4, it is seen that zero crossing points of transmitter current (pink) and half bridge switching node voltage (green) are almost equal for 400 kHz design. Therefore, it can be said that operation is at ZPA. However, for 500 kHz design, phase difference between transmitter current and half bridge switching node voltage is higher as can be seen in Figure 6.5. The phase shift can be due to the resonant capacitor tolerance. This phase difference is neglected because it is around 80 ns, which is much smaller than the period, 2 μs.

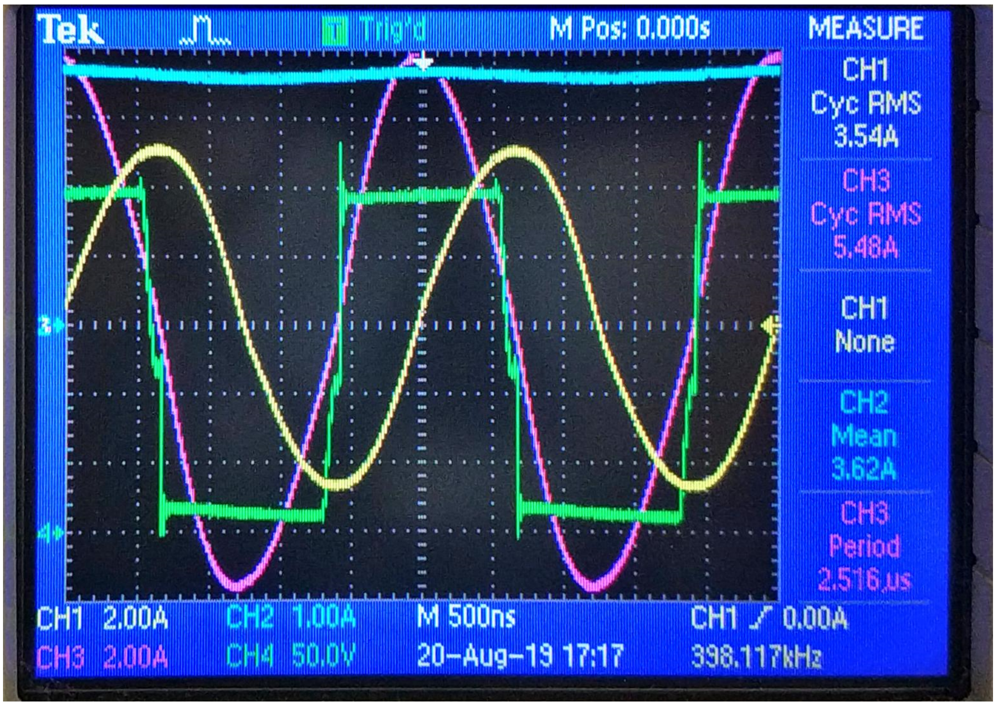

Figure 6.4: Oscilloscope screen for 400 kHz test with filtered resistive load, yellow (CH1): receiver coil current, blue (CH2): rectified and filtered load current, pink (CH3): transmitter coil current, green (CH4): half bridge switching node voltage

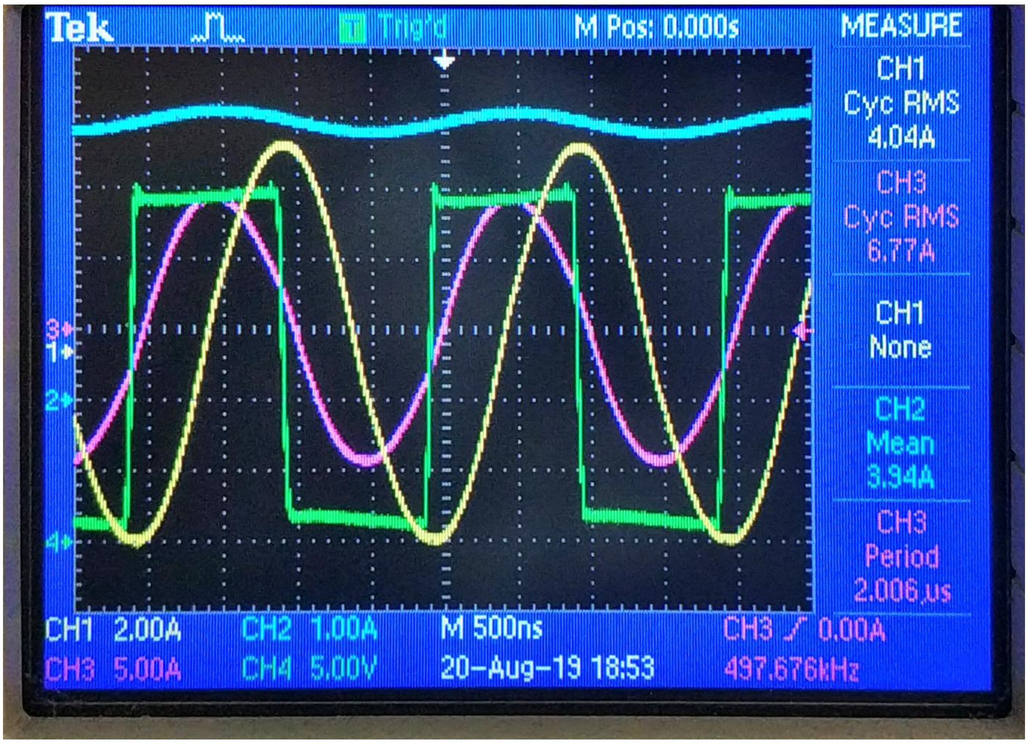

Figure 6.5: Oscilloscope screen for 500 kHz test with filtered resistive load, yellow (CH1): receiver coil current, blue (CH2): rectified and filtered load current, pink (CH3): transmitter coil current, green (CH4): half bridge switching node voltage

6.4 Loss Analysis

In the previous section, all related data is given. Now, it is better to calculate losses and show loss distributions. While calculating the losses, measured resistances of coils at corresponding resonance frequency were used. For the semiconductors, switching losses at the primary half bridge is neglected because operating at resonance frequency means switching at nearly zero current. Therefore, only conduction loss is considered while calculating MOSFETs' losses. On state resistance of primary side MOSFET (CSD19531Q5A) is taken as 7 $m\Omega$ from its datasheet within the consideration of temperature and gate-source voltage. For rectifier diodes (V12P10) on state voltage drop is taken as 0.5 V by using its datasheet within the consideration of temperature and current passes through it.

Loss distribution are shown in Table 6.3 and Table 6.4. Moreover, the results are visualized and compared by using bar charts in Figures 6.6, 6.7, 6.8, 6.9, 6.10 and 6.11.

Table 6.3: Loss distribution of the design with 400 kHz resonance frequency

	Resistive load				Resistive load with pi filter			
	Test 1	Test 2	Test 3	Test 4	Test 1	Test 2	Test 3	Test 4
Output power (W)	50.8	69.4	51.8	29.3	38.4	51.2	44.7	21.9
Tx coil loss (W)	7.6	22.8	16.3	3.9	3.7	13.3	9.6	2.1
Rx coil loss (W)	2.9	3.4	2.9	1.8	2.5	3.45	3	1.7
MOSFET loss (W)	0.4	1.3	0.9	0.2	0.21	0.78	0.5	0.12
Diode loss (W)	-	-	-	-	3.6	4.2	3.9	2.75
Output power + losses (W)	61.6	86.8	71.9	35.2	48.5	72.8	61.7	28.6
Input power (W)	66	86.2	72.9	35.5	47.7	68.5	58.3	27.5

Table 6.4: Loss distribution of the design with 500 kHz resonance frequency

	Resistive load				Resistive load with pi filter			
	Test 1	Test 2	Test 3	Test 4	Test 1	Test 2	Test 3	Test 4
Output power (W)	57.6	69.6	57.5	34.1	45.9	59.6	48.4	26.3
Tx coil loss (W)	8.7	29.4	18.3	5.34	4.95	17.4	10.7	2.9
Rx coil loss (W)	2.5	3	2.5	1.48	2.5	3.27	2.65	1.4
MOSFET loss (W)	0.56	1.9	1.18	0.35	0.11	1.13	0.69	0.06
Diode loss (W)	-	-	-	-	3.94	4.5	4.1	3
Output power + losses (W)	69.4	103.9	79.4	41.3	57.4	85.9	66.4	33.6
Input power (W)	74	100.6	79.3	44	57.5	82.4	64.3	33.4

In Tables 6.3 and 6.4, output power values and input power values for both designs are the measured values whereas the other loss components are the estimated values by using corresponding currents and other parameters, such as on-state resistance of MOSFET and on-state voltage drop of diode. As seen in both tables, measured input power value coincides with the estimated input power which is the sum of the output power and losses. Therefore, it can be said that estimated losses have a pretty good accuracy.

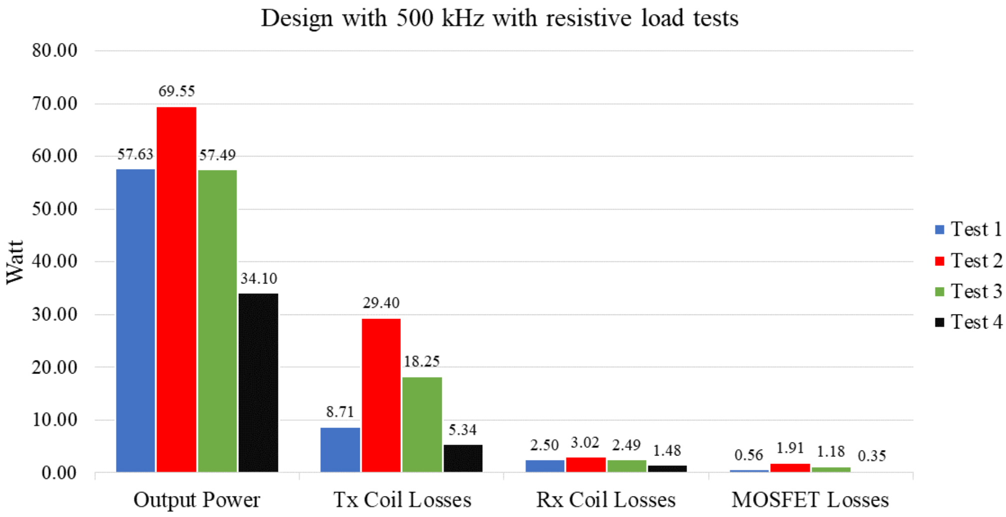

Figure 6.6: Loss distribution of the design with 500 kHz resonance frequency with resistive load

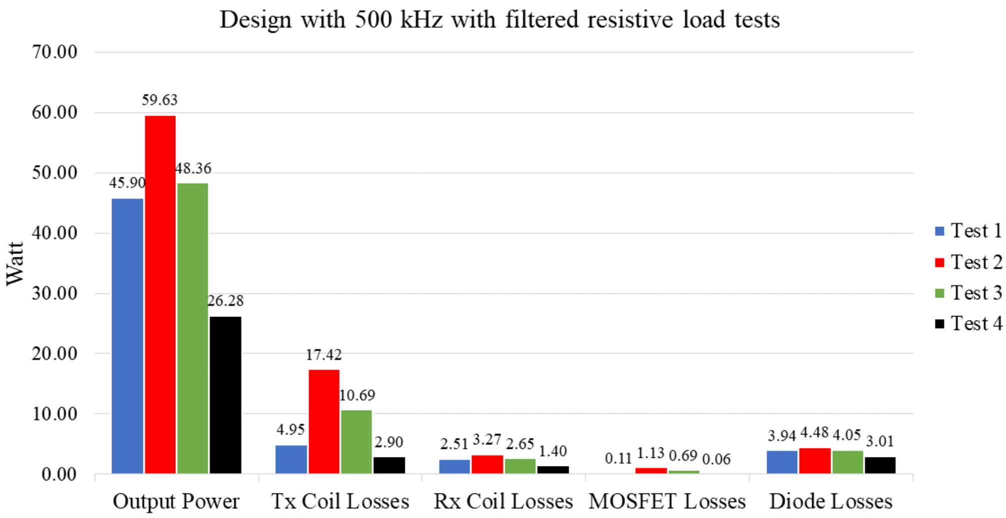

Figure 6.7: Loss distribution of the design with 500 kHz resonance frequency with filtered resistive load

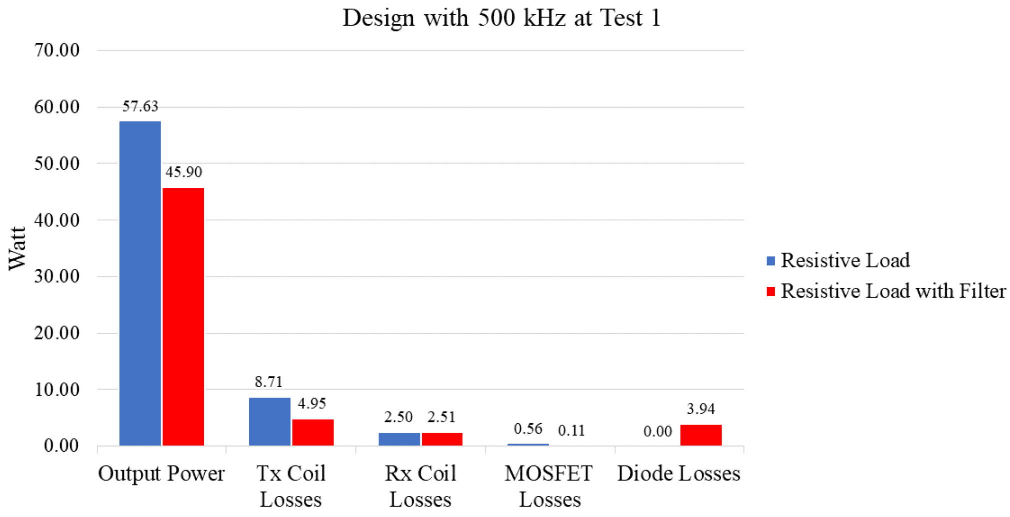

Figure 6.8: Loss comparison for resistive load and filtered resistive load of the design with 500 kHz resonance frequency for Test 1

Considering the loss components, it can be seen that the most dominant loss component is the transmitter coil loss. For the design with 500 kHz resonance frequency, at nominal case with resistive load, 8.71 W transmitter coil loss, which corresponds ∼12.5% efficiency degradation, is calculated as seen in Figure 6.6. For the misalignment cases, transmitter coil loss increases up to 29.4 W as seen in the same figure. Measured transmitter coil loss is much higher than the expected loss. This is caused by the miscalculation of the transmitter coil resistance. Therefore, in order to have a better design in terms of efficiency, resistance calculation of the coils should be more accurate.

MOSFET losses and receiver coil losses are more reasonable than the transmitter coil losses as in Figure 6.6. However, when the system is tested with filtered resistive load, extra semiconductors, rectifier diodes, are added to the system and ∼4 W loss is obtained on those diodes. Again, 4 W loss is pretty high for a semiconductor. To solve this problem, a better cooling method can be applied. Another solution can be using MOSFETs instead of diodes. If MOSFETs are used in ideal diode emulation mode, overall loss can be decreased.

Another discussion point is the effect of filtering. No change was expected in receiver coil currents and this is validated because receiver coil losses for both case in both Figure 6.8 and Figure 6.11 are almost equal for resistive load and filtered resistive load tests. This means that receiver coils have no change as expected. Expected effect of the filtering is to lower output power and consequently transmitter coil losses, and this is also validated.

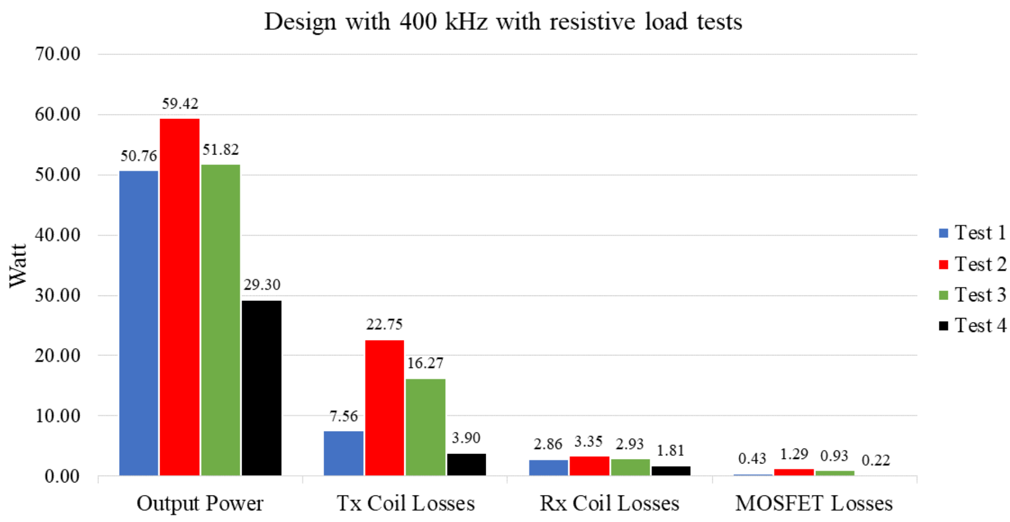

Figure 6.9: Loss distribution of the design with 400 kHz resonance frequency with resistive load

Same comments for the design with 500 kHz resonance frequency are valid for the design with 400 kHz resonance frequency as can be seen in Figures 6.9, 6.10, 6.11.

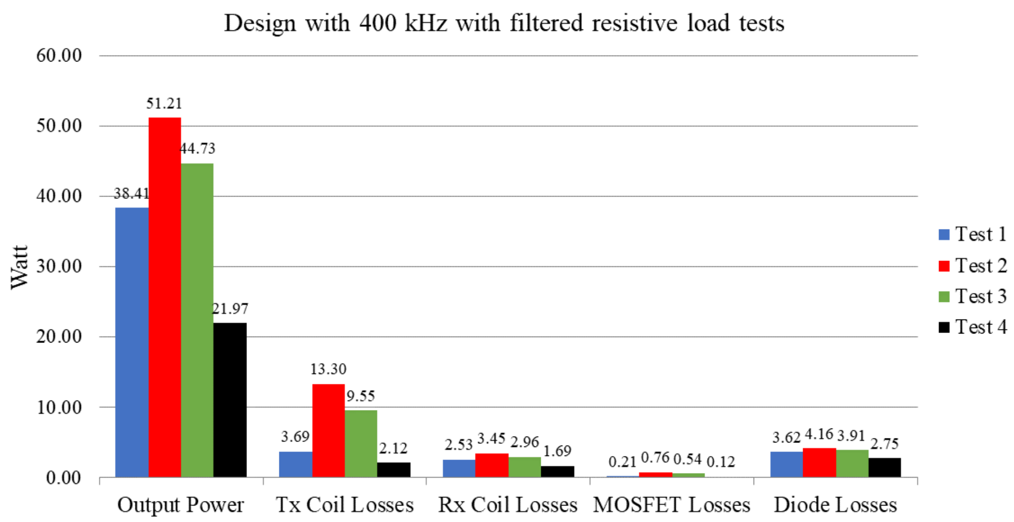

Figure 6.10: Loss distribution of the design with 400 kHz resonance frequency with filtered resistive load

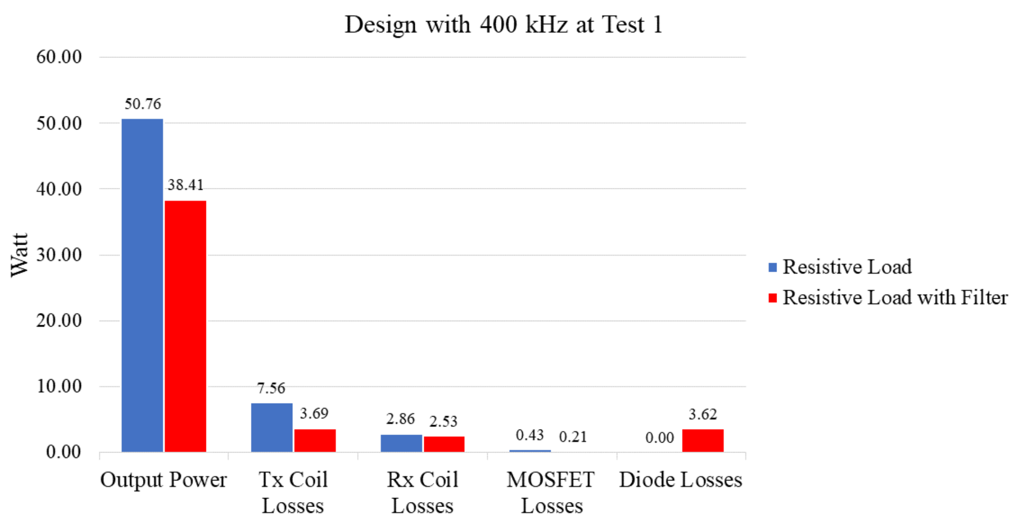

Figure 6.11: Loss comparison for resistive load and filtered resistive load of the design with 400 kHz resonance frequency for Test 1

CHAPTER 7

SHIELDING

One of the main problem of WPT applications is the generated magnetic field. It may be coupled with any surrounding environment such as an electrical device and that device may be interfered by the field. In addition to effect on other electrical devices, coupling to a foreign conductive material, i.e. a coin, can easily lead to an excessive amount of temperature increase. Besides of these effects, magnetic field exposure on a human body is another critical point that must be restricted. Therefore, magnetic fields must be compliant with the Electromagnetic Field safety standards as defined in [28], [13] for human exposure, or it must be compliant with the electromagnetic compatibility restrictions in order to lower interference effects to other electrical devices.

Shields must be designed to meet magnetic field restrictions, however effect of shielding to the electrical performance is another point that must be taken into account. Shielding may improve or degrade the performance of the WPT system. In this chapter, shielding requirements to meet the magnetic field regulations according to the ICNIRP will be mentioned. Effect of shield to the system performance will be studied and shielding performance of different materials will be analyzed by using ANSYS Maxwell.

7.1 Shield Requirements

Wearable WPT applications or implantable WPT applications directly lead magnetic field exposure on the human body. Therefore, such applications must be compliant with the regulations of ICNIRP. In Figure 7.1, magnetic field limitations according to the regulations of ICNIRP with respect to occupational and general public applications are shown. Since application in this thesis is in occupational area, occupational limitations are used. In the following subsections, FEA simulations and shield performances will be analyzed by using information in Figure 7.1.

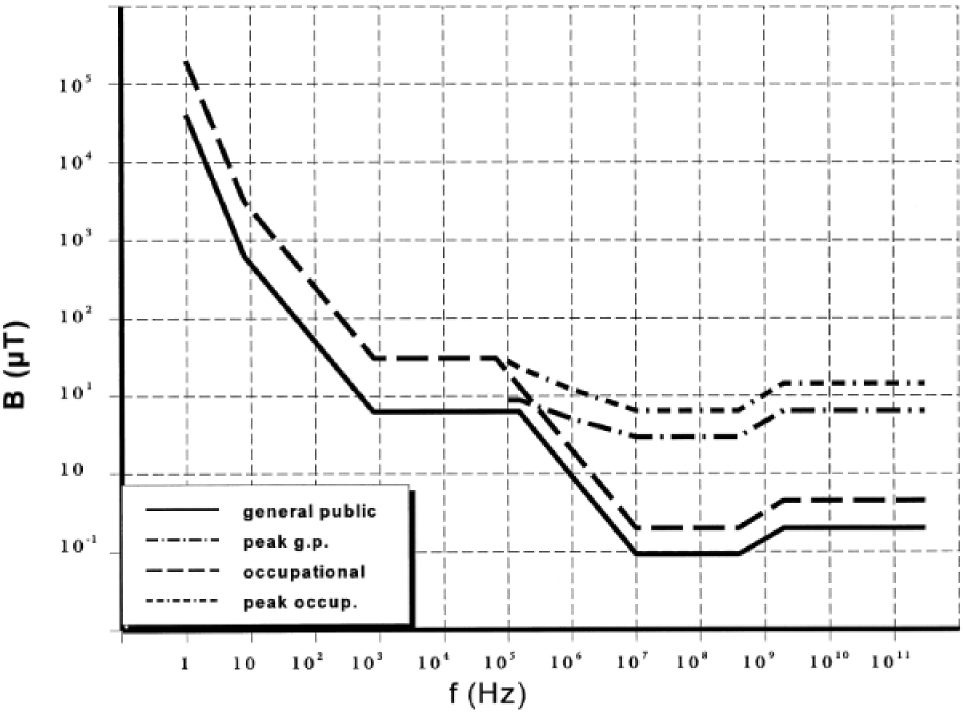

Figure 7.1: Reference levels for exposure to time varying magnetic fields [13]

7.2 Shield Effects on Wireless Power Transfer

Magnetic or conductive materials are mostly used for passive shielding. Shields can be designed out of good conductors such as copper and aluminum or magnetic materials with very low conductivity such as ferrites. Based on the used material, there are two main shielding methods that are conductive and magnetic shielding [29].

Conductive shielding is based on Faraday's law. Time-varying magnetic field creates electromagnetic force and it leads to induce eddy current on the shield that cancels the incident magnetic field [24]. As a concequence, the overall magnetic field is reduced and therefore WPT performance is degraded due to the power loss in the conductive shield [30]. Not only the power loss on conductive shield degrades the performance of WPT, created magnetic field, which is opposing the incident one by eddy current lowers the self-inductance of the coils and consequently lowers the coupling between transmitter and receiver coils. This is another cause of degradation of WPT performance.

On the contrary to the blocking the incident magnetic field behaviour of conductive shielding, shields with magnetic materials divert or redirect the magnetic field. In other words, it provides a preferential path for the magnetic flux lines [24]. Because reluctance of the magnetic flux lines' path is lowered by magnetic material, self-inductance of the coils increases and consequently, coupling between transmitter and receiver coil increases. Finally, WPT performance is improved.

Since using conductive shield degrades the performance of the WPT system, magnetic shield is studied in terms of performance variation and shielding performance in this chapter. In order to improve shielding performance, a hybrid (magnetic+conductive) shield combination is also studied.

7.3 Shield Performance

In order to observe the effect of ferrite shield on self and mutual inductance of the coils, a 2D-FEA model is constructed as shown in Figure 7.2. Transmitter coil turns are shown with yellow circles and placed on x-axis. Receiver turns are shown with 6 green circles. Ferrite shield is placed 1 mm away from the coils and shield thickness is increased until it doesn't get saturated by the magnetic field created by the coils. Shield material is assumed to have a relative permeability of 3000 until 0.5 T and its conductivity is neglected. As simulation results, self inductances for transmitter and receiver coils and mutual inductances are obtained. Corresponding FEA simulation results and their comparison with unshielded cases are in Table 7.1

As seen in Table 7.1, self and mutual inductances increase significantly with ferrite shield. With the new improved system, in order to have the same amount of required output power, resonance frequency is required to be lowered. New resonance frequencies can be seen in Table 7.1. So, FEA models are simulated for two different design

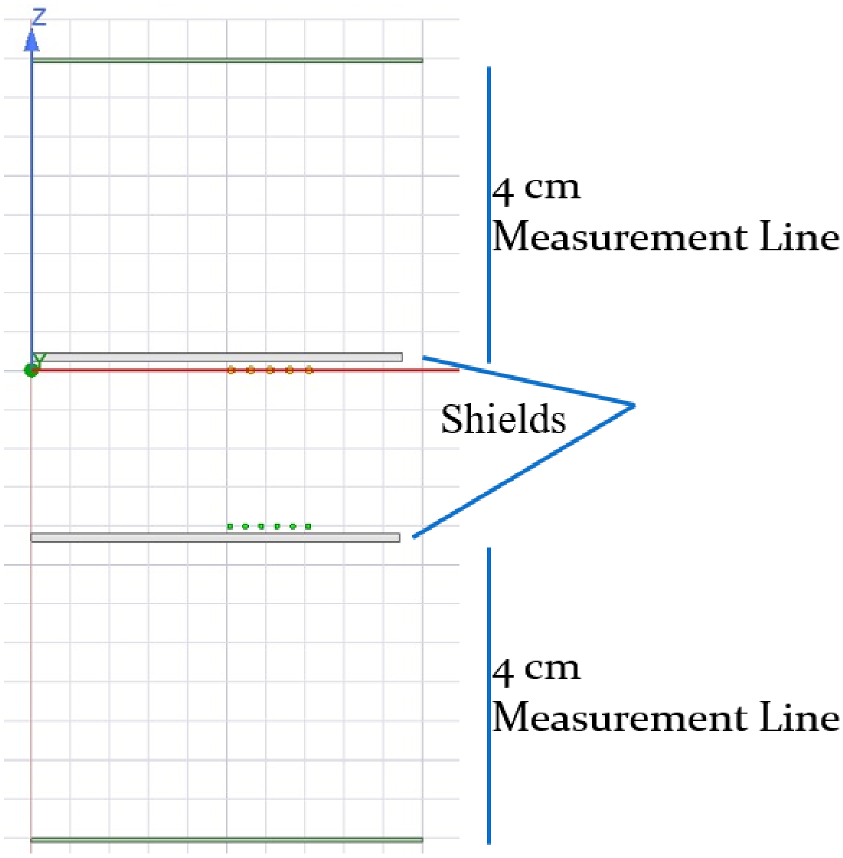

Figure 7.2: 2D-FEA model for shield performance measurement

Table 7.1: Magnetic shielding effect on self and mutual inductance

	Design with 500 kHz		Design with 400 kHz	
	W/o magnetic shield	W/ magnetic shield	W/o magnetic shield	W/ magnetic shield
Tx self inductance (μH)	2.49	4.12	3.06	5.05
Rx self inductance (μH)	3.63	6.08	4.86	8.41
Mutual inductance (μH)	0.77	1.75	1.06	2.44
Resonance frequency (kHz)	500	220	400	155

cases, 500 kHz resonance frequency and 400 kHz resonance frequency, but they are simulated for their new resonance frequencies, 220 kHz and 155 kHz, respectively.

To start with, shields with only ferrite material are tested. During simulations, ferrite thickness is limited to 10 mm due to space and weight limitations. In order to find a proper shielding that fulfills the magnetic field limitations shown in Figure 7.1, ferrite thickness is swept from 0.1 mm to 10 mm and its performance is observed. For this application, since the receiver part will be wearable, the minimum distance between the receiver coil and the human is taken as 4 cm. Therefore, magnitude of the B field is observed at 4 cm away from receiver coils.

In Figure 7.3, red line is the limit for maximum B field that is 27 μT and B fields for ferrite shield for both case are above the limits. Therefore, hybrid (ferrite+aluminum) shielding performance for both cases is analyzed. For this test, again thickness of the ferrite is swept from 0.1 mm to 10 mm. However, thickness of aluminum is fixed to 3 times of the skin depth at corresponding resonance frequencies. This is because of the fact that significant part of the eddy current flows on the surface and as the aluminum thickness increase, shielding performance of it improves but improvement of the shielding is not linear with thickness because eddy currents in the inner parts of the conductor decrease exponentially.

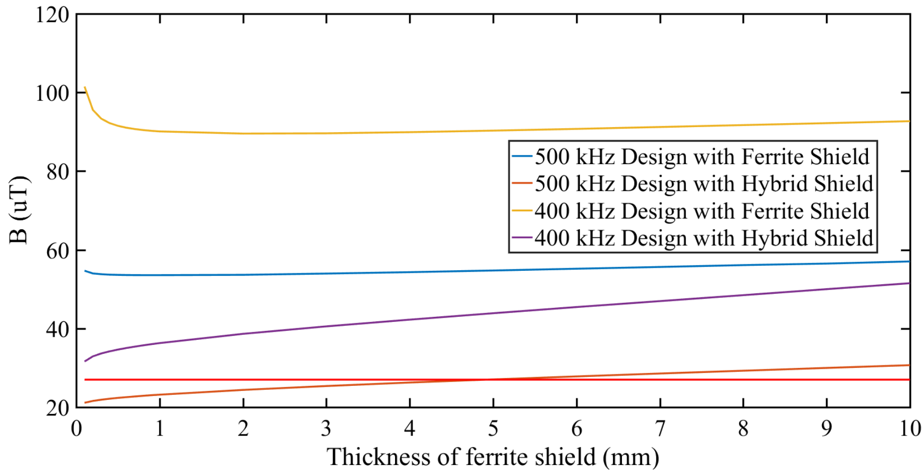

Figure 7.3: Shielding performance with respect to thickness of ferrite shield

As seen in Figure 7.3, hybrid shielding is much more effective than ferrite shielding. For different design comparison, it can be concluded as higher frequency can be shielded much easier than the lower frequency.

In this case, only the design with 220 kHz resonance frequency with shielding is compatible with the ICNIRP standards. Therefore, it can be concluded that shielding is one of the most essential points in WPT systems. In addition, since the shielding affects the performance of the system, its effect must be taken into account from the beginnings of the design procedure.

CHAPTER 8

CONCLUSION

A design procedure is followed step by step in order to design and implement a 50 W wireless battery charger for a vest application in this thesis. As the first step, wireless power transfer method is studied and inductive power transfer method is selected based on the power transfer distance requirement and the frequency limitation. In the second step, basic compensation topologies are studied and Series-Series (SS) is found as the most suitable topology for the battery charger application. Ease of driving the switching circuit, stability of the system over misalignment are the main reasons why SS topology is selected. For the next step of the design, planar spiral coil structure is selected for transmitter and receiver because of its compact design and calculation of resistance, self inductance and mutual inductance of coils is studied and verified by using ANSYS Maxwell. As the final step of the design procedure, Pareto-front search is applied and two different coil pairs are determined.

Selected two designs are simulated by using PLECS circuit simulation tool and a battery charging solution is applied in the simulations. Simulated designs are implemented and tested. As test results, theoretical expectations such as efficiency and other expectations that are observed on simulations such as filtering effect and misalignment effect of bifurcation are verified.

In the final part of the thesis, shielding requirements for this wearable applications are studied. In addition, different passive shielding methods, magnetic, conductive and hybrid shielding methods, are mentioned and their effects on WPT performance are analyzed. Shielding performances of magnetic material shielding and hybrid shielding are obtained by using FEA simulation tools and their performances are compared. Performance of the magnetic shielding is quite good but not enough for this application. However, hybrid shielding is found as a much better shielding method than magnetic shielding.

Since the followed design procedure relies on the Pareto-front search, accurate calculation of the resistance and inductance values are the most critical points because a miscalculation in these values leads to a worse design than expected. In this thesis, the calculated resistance of the Litz wire is much lower than its actual value. Therefore, measured efficiency is less than expected. Consequently, Litz wire resistance estimation can be left as a point that needs improvement. Another point that may need improvement in this thesis is the operating frequency. Incresing operating frequency would allow higher transferred power for the same transfer distance or larger transfer distance for the same amount of power. Also, shielding topic is only studied in the simulation environment. Magnetic and conductive shields can be implemented and tested to validate effect of them on the system performance and their shielding performances can be evaluated by using gauss meters.

REFERENCES

[1] Jesús Sallán, Juan L Villa, Andrés Llombart, and José Fco Sanz. Optimal design of icpt systems applied to electric vehicle battery charge. *IEEE Transactions on Industrial Electronics*, 56(6):2140–2149, 2009.

[2] Kunwar Aditya and Sheldon S Williamson. Design considerations for loosely coupled inductive power transfer (ipt) system for electric vehicle battery charging-a comprehensive review. In *2014 IEEE Transportation Electrification Conference and Expo (ITEC)*, pages 1–6. IEEE, 2014.

[3] Ravikiran Vaka and Ritesh Kumar Keshri. Review on contactless power transfer for electric vehicle charging. *Energies*, 10(5):636, 2017.

[4] Andre Kurs, Aristeidis Karalis, Robert Moffatt, John D Joannopoulos, Peter Fisher, and Marin Soljačić. Wireless power transfer via strongly coupled magnetic resonances. *Science*, 317(5834):83–86, 2007.

[5] Fei Lu, Hua Zhang, and Chris Mi. A review on the recent development of capacitive wireless power transfer technology. *Energies*, 10(11):1752, 2017.

[6] CLW Sonntag, EA Lomonova, and JL Duarte. Variable-phase contactless energy transfer desktop part i: Design. In *2008 International Conference on Electrical Machines and Systems*, pages 4460–4465. IEEE, 2008.

[7] Peter D Bradley. Wireless medical implant technology—recent advances and future developments. In *2011 Proceedings of the European Solid-State Device Research Conference (ESSDERC)*, pages 54–58. IEEE, 2011.

[8] Juan Luis Villa, Jesús Sallán, Andrés Llombart, and José Fco Sanz. Design of a high frequency inductively coupled power transfer system for electric vehicle battery charge. *Applied Energy*, 86(3):355–363, 2009.

[9] ANSYS. Modeling wireless power transfer in ANSYS. 2017.

[10] Chwei-Sen Wang, Grant A Covic, and Oskar H Stielau. Power transfer capability and bifurcation phenomena of loosely coupled inductive power transfer systems. *IEEE Transactions on Industrial Electronics*, 51(1):148–157, 2004.

[11] Jesús Acero, Rafael Alonso, José M Burdío, Luis A Barragan, and Diego Puyal. Frequency-dependent resistance in litz-wire planar windings for domestic induction heating appliances. *IEEE Transactions on Power Electronics*, 21(4):856–866, 2006.

[12] Anele O Amos, Hamam Ykandar, Alayli Yasser, and Djouani Karim. Computation of the mutual inductance between circular filaments with coil misalignment. In *2013 Africon*, pages 1–5. IEEE, 2013.

[13] ICNIRP Guideline. Guidelines for limiting exposure to time-varying electric, magnetic, and electromagnetic fields (up to 300 ghz). *Health Physics*, 74(4):494–522, 1998.

[14] Nikola Tesla. Apparatus for transmitting electrical energy., December 1 1914. US Patent 1,119,732.

[15] Chun T Rim and Chris Mi. *Wireless power transfer for electric vehicles and mobile devices*. John Wiley & Sons, 2017.

[16] Surajit Das Barman, Ahmed Wasif Reza, Narendra Kumar, Md Ershadul Karim, and Abu Bakar Munir. Wireless powering by magnetic resonant coupling: Recent trends in wireless power transfer system and its applications. *Renewable and Sustainable energy reviews*, 51:1525–1552, 2015.

[17] Xuezhe Wei, Zhenshi Wang, and Haifeng Dai. A critical review of wireless power transfer via strongly coupled magnetic resonances. *Energies*, 7(7):4316–4341, 2014.

[18] Eugenio Culurciello and Andreas G Andreou. Capacitive inter-chip data and power transfer for 3-d vlsi. *IEEE Transactions on Circuits and Systems II: Express Briefs*, 53(12):1348–1352, 2006.

[19] Daniel C Ludois and Justin K Reed. Brushless mitigation of bearing currents via capacitively coupled shunting. In *2014 International Conference on Electrical Machines (ICEM)*, pages 2336–2342. IEEE, 2014.

[20] Chaoyun Song, Ana López-Yela, Yi Huang, Daniel Segovia-Vargas, Yuan Zhuang, Yansong Wang, and Jiafeng Zhou. A novel quartz clock with integrated wireless energy harvesting and sensing functions. *IEEE Transactions on Industrial Electronics*, 66(5):4042–4053, 2018.

[21] Chwei-Sen Wang, Oskar H Stielau, and Grant Covic. Design considerations for a contactless electric vehicle battery charger. 2005.

[22] Juan L Villa, Jesus Sallan, José Francisco Sanz Osorio, and Andrés Llombart. High-misalignment tolerant compensation topology for icpt systems. *IEEE Transactions on Industrial Electronics*, 59(2):945–951, 2011.

[23] JPK Sampath, A Alphones, LYY Kenneth, and DM Vilathgamuwa. Analysis on normalized distance and scalability in designing wireless power transfer. In *2015 IEEE PELS Workshop on Emerging Technologies: Wireless Power (2015 WoW)*, pages 1–6. IEEE, 2015.

[24] Mauro Feliziani and Silvano Cruciani. Mitigation of the magnetic field generated by a wireless power transfer (wpt) system without reducing the wpt efficiency. In *2013 International Symposium on Electromagnetic Compatibility*, pages 610–615. IEEE, 2013.

[25] Jan Abraham Ferreira. *Electromagnetic modelling of power electronic converters*. Springer Science & Business Media, 1989.

[26] Milton Abramowitz and Irene A Stegun. *Handbook of mathematical functions with formulas, graphs, and mathematical tables*, volume 55. US Government printing office, 1948.

[27] Jinwook Kim and Young-Jin Park. Approximate closed-form formula for calculating ohmic resistance in coils of parallel round wires with unequal pitches. *IEEE Transactions on Industrial Electronics*, 62(6):3482–3489, 2014.

[28] D ICNIRP. Guidelines for limiting exposure to time-varying electric and magnetic fields (1 hz to 100 khz). *Health Physics*, 99(6):818–836, 2010.

[29] Sukjin Kim, Daniel H Jung, Jonghoon J Kim, Bumhee Bae, Sunkyu Kong, Chiuk Song, and Joungho Kim. Modeling of electromagnetic interference

shielding materials in wireless power transfer for board-to-board level interconnections. In *2014 IEEE Wireless Power Transfer Conference*, pages 273–276. IEEE, 2014.

[30] Tommaso Campi, Silvano Cruciani, and Mauro Feliziani. Magnetic shielding of wireless power transfer systems. In *2014 International Symposium on Electromagnetic Compatibility, Tokyo*, pages 422–425. IEEE, 2014.